ABSTRACT

Title of Thesis: BATTERY POWERED PORTABLE VAPOR COMPRESSION CYCLE SYSTEM WITH PCM CONDENSER

Yilin Du, Master of Science, 2016

Thesis Directed By: Research Professor, Yunho Hwang, Department of Mechanical Engineering

A battery powered air-conditioning device was developed to provide an improved thermal comfort level for individuals in inadequately cooled environments. This device is a battery powered air-conditioning system with the phase change material (PCM) for heat storage. The condenser heat is stored in the PCM during the cooling operation and is discharged while the battery is charged by using the vapor compression cycle as a thermosiphon loop. The main focus of the current research was on the development of the cooling system. The cooling capacity of the vapor compression cycle measured was 165.6 W with system COP at 2.85. It was able to provide 2 hours cooling without discharging heat to the ambient. The PCM was recharged in nearly 8 hours under thermosiphon mode.

BATTERY POWERED PORTABLE VAPOR COMPRESSION CYCLE SYSTEM WITH PCM CONDENSER

by

Yilin Du

Thesis submitted to the Faculty of the Graduate School of the
University of Maryland, College Park, in partial fulfillment
of the requirements for the degree of
Master of Science
2016

Advisory Committee:

Research Professor Yunho Hwang, Chair

Professor Jelena Srebric

Associate Professor Bao Yang

Acknowledgements

I would like to give my sincere thanks to Center for Environmental Energy Engineering, which provides me the resources and opportunity to conduct the challenging project for my thesis. Thanks to my research advisor Dr. Yunho Hwang, he also gave creative ideas and academic support to this project. I also want to give my thanks to Dr. Reinhard Radermacher and Dr. Vikrant Aute, who provided continuous guidance and passions for this project.

I want to express deepest thanks to my fiancé, Chengliang Lian, and my parents. I always feel their love and warm support during my difficult times. I wouldn't successfully finish my work without my families' support.

Thanks to other staff in CEEE. Great thanks to Jan Muehlbauer, his expertise in test facilities helped me develop the prototype and finish the test for this thesis. Discussions with Dr. Jiazhen Ling and Dr. Hoseong Lee also gave me new ideas. Special thanks to Manjie Li. She helped me a lot during my first year, which prepared me well to finish the thesis work.

Finally, I want to give my sincere thanks to University of Maryland. It is a fantastic experience here to study for my Master degree.

Table of Contents

List of Tables

List of Figures

Nomenclature

D	Tube Inner Diameter
f	Fanning Factor
g	Acceleration of the Gravity
L	Tube Length
h	Heat Transfer Coefficient
Nu	Nusselt Number
p	Pressure
Pr	Prandtl number
Re	Reynolds Number
V	Velocity

Greek symbols

μ	Dynamic Viscosity
ρ	Density
ε	Void Fraction

Subscript

f	Fluid
g	Gas
liq	Liquid
LT	Assuming All Mass Flowing as Liquid
rand	Random

sys	System
tp	Two-Phase
vap	Vapor
x	Vapor Quality

Abbreviation

Avg.	Average
CFM	Cubic Feet per Minute
CLTPT	Closed Loop Two-Phase Thermosiphon
Comp.	Compressor
Cond.	Condenser
COP	Coefficient of Performance
DAQ	Data Acquisition
DC	Direct Current
Evap.	Evaporator
HTC	Heat Transfer Correlation
MFM	Mass Flow Meter
NI	National Instrument
Ref.	Refrigerant
RH	Relative Humidity
RPM	Revolution per Minute
PCM	Phase Change Material
PVC	Polyvinyl Chloride

PWM	Pulse Width Modulation
TC	Thermocouple
Temp.	Temperature
USDA	U.S. Department of Agriculture
VCC	Vapor Compression Cycle

Chapter 1: Introduction

1.1 Background

Space cooling is essentially important for occupants as it provides thermal comfort while it takes up a large portion of the total energy consumption in the U.S. According to Annual Energy Outlook 2015 [1], in 2013, the energy consumption in space cooling for commercial sector was 451.3 TWh per year, which made up to 8.5% of the total energy consumption. While for the residential sector, the energy consumption was 600.8 TWh per year and counted for 9.7% of the total energy consumed. This section of energy keeps increasing for both commercial and residential section. The estimated energy consumption in 2020 is 477.7 TWh and 697.5 TWh per year for commercial and residential sections, respectively.

A simple way to save energy for space cooling in hot summer is to turn the thermostat settings in building up to a higher setting. It helps save energy by 1%-3% per degree, for each degree the thermostat is set above 22.2°C [2]. However, it may result in the thermal discomfort to some people with higher metabolic rate or doing heavy work. Instead of turning the thermostat down for the whole space, another more efficient way is to adopt personal cooling devices.

In addition to improving thermal comfort level and saving the energy used for space cooling, personal cooling is also important for people exposed to extreme conditions. During 2006-2012, 3,332 U.S. residents died due to the exposure to the excessive natural heat, which accounts for 31% of the total death associated with weather-related causes [3].

1.2 Objective

The objective of this thesis is to design, build and test a battery powered portable vapor compression cycle person cooling system (referred as RoCo in the thesis). The target working environment for this device is the indoor environment like office or residential buildings. Therefore, the heat from the condenser needs to be stored within the system. For this reason, the PCM is proposed to store condenser heat. The recharging process of the PCM is another challenge after the cooling mode. A novel thermosiphon design is integrated with the vapor compression cycle to resolve the PCM recharging process. After designing the RoCo, the laboratory prototype is constructed to prove the concept. Then the experimental work is conducted to validate the performance. Experimental work is conducted in two stages: one is the baseline test. A test facility with full instruments is set up to measure the detailed temperature, pressure, mass flow rate and power consumption of the refrigerant system. Both the vapor compression cycle and thermosiphon loop are tested and validated in this stage. The second stage is to integrate the cooling system with a portable platform and nozzle and build the prototype. The system performance of the prototype is evaluated and compared with the baseline test.

Chapter 2: Literature Review

2.1 Personal Cooling

General personal cooling devices use technologies like forced convection air cooling, evaporative cooling, phase change materials, thermoelectric cooling or vapor compression cycles.

The mechanism of forced convection air cooling is to increase the sensible heat transfer and the water vaper pressure gradient between the skin and environment, thus accelerating the sweat evaporation [4]. The most common forced convection air cooling devices for personal cooling are portable fans. Products like Cool on the Go [5] are available in market. Forced convection air cooling is also used in vest under extreme conditions. McLellan [6] conducted an experimental study on the efficacy of an air-cooling vest designed for light armor vehicle personnel, who were subjected to high ambient temperature. The vest was made of two layers of air-impermeable urethane-coated nylon and 20.3°C and 12.1°C cool air were supplied from a heat exchanger immersed in cool water reservoir at 49°C and 35°C exposure temperatures, respectively. After 3 hours test, the ratings of thermal comfort improved to 7.6 and 5.7 from 9.7 and 9 for 35°C and 49°C temperature settings. This research showed improvement of thermal comfort level and reduction of thermal strain under extreme weather conditions. However, it required extra cold water supply and the cooling vest also added thermal resistance without cold water supply.

Evaporative cooling takes advantage of the large latent heat of water. Portable evaporative coolers are available in the market. The evaporative cooler usually equips

with a water tank and is able to provide a cool air using a natural evaporative cooling process.

Phase change materials are used to store latent heat. Compared with sensible heat storage, latent heat storage has higher storage density while the material maintains its temperature during heat storage and release process [7]. PCM integrated into the vest is a promising technology for personal cooling and the solidification process of PCM after use needs to be considered. Ice is a cheap option to serve as PCM in the vest. However, the low melting temperature of ice may cause erythema and thus discomfort and extra electricity consumption of freezer is required for solidification [8]. Kuklane et al. [9] proposed to use other types of PCMs with higher melting temperature (around 20°C), like Glauber's salt or organic hydrocarbons/wax. Thus the melted PCM can be solidified using underground/well water instead of freezer. The impact of different melting temperature on heat stress was also studied [8]. The melting temperature of the PCMs in the cooling vest changed from 0°C, 10°C, 20°C and 30°C and the test was conducted under 40°C dry bulb temperature and 46% RH. The results suggested that 0°C was too cold and shouldn't be used without additional insulation. 10°C melting temperature PCM was additionally preferred by the participants. The service time of the cooling vest depends on the total capacity of the PCM integrated. Thus extended service hours require larger amount the PCM and the vest becomes bulky and heavy. Besides, solidification of PCM is required after use and may require more time and extra energy. The transportation of replacement PCM packs is also cumbersome [10].

Thermoelectric technology is used in C2 climate control [11], a personal climate-control device product by Herman Miller. It is designed to be aimed at face and neck. With a baseline temperature of 22.2°C, it is able to provide cooling and heating between 66°F to 112°F. However, the capacity of it is not sufficient to be used alone without air-conditioning or space heating systems.

Traditional vapor compression cycle is popular in small air conditioning appliances for personal cooling, like portable air conditioning. Vapor compression cycle was also applied in wearable cooling systems for military, firefighting or other hazardous duty personnel working under elevated temperature environments [12]. An engine-driven R-134a miniaturized compressor was used in the system and it was able to provide 178 W of cooling for 5.7 hours under ambient temperature range of 37.7-47.5°C. Compared with other technologies, the vapor compression cycle is able to provide an extended and stable cooling effect based on limited components and flexibility.

2.2 Heat Exchanger Integrated with PCM

Thermal energy storage is a promising technology because it helps balance the energy supply and demand by storing extra thermal energy for future use. The form of thermal energy stored can be sensible heat or latent heat, depending on whether the materials for thermal energy storage undergo a temperature change or phase change process.

PCM is used in the latent heat thermal energy storage systems. Typically the system has three main components: PCM with suitable temperature range, encapsulation of PCMs and a heat exchange surface required for transferring the heat from heat source

to PCM or from PCM to the heat sink [13]. In this section, the research is focused on the experimental work for the heat exchanger integrated with PCM.

One main challenge of using PCM as thermal storage material is the low thermal conductivity of PCM. For organic PCMs, the paraffin has a low thermal conductivity at around 0.2 W/(m·K) while non-paraffin suffers from even lower range from 0.15 to 0.17 W/(m·K) [14]. Inorganic PCMs have higher thermal conductivity and some of the products are available in market [15] even with a thermal conductivity of 1 W/(m·K). Medrano et al. [16] summarized that there were different technologies to enhance the heat transfer between PCMs and heat changers due to low thermal conductivity: inserting the PCM in a metal; adding high thermal conductivity metallic particles; macro and micro encapsulating the PCM; using PCM-graphite composite material; and using finned tubes with different configurations.

Trp [17] conducted experiments to study the melting and solidification processes of paraffin in a shell-and-tube heat exchanger. The melting temperature of the paraffin was 27.5°C with thermal conductivity of 0.18 W/(m·K) and 0.19 W/(m·K) for solid and liquid phases, respectively. The experiment showed that the melting process of PCM was non-isothermal as the melting temperature was in a range of 22°C to 37°C while the solidification process was isothermal with narrow solidification temperature of 27.5°C to 28°C.

Erek et al. [18] also investigated the performance of a shell-and-tube heat exchanger with pure water as PCM filling the annular shell space. Instead of using the bare tube, he employed finned tube in the experiment. The numerical model was developed as well and it showed that Reynolds number of heat transfer fluid had a dominant effect

on energy storage rate while higher fin density and lower fin spacing also contributed to the increased energy storage rate.

Medrano et al. [16] studied five cases of small commercial heat exchangers used as PCM thermal storage system: a double pipe copper tube heat exchanger with PCM in annular space; the same double pipe heat exchanger with PCM embedded in graphite matrix; a double pipe heat exchanger with 13 radial copper fins; aluminum-fins-and-copper-tube heat exchanger with PCM filled in the space between tubes and fins; and a small Alfa Laval gasketed plane and frame heat exchanger. The PCM used in this study was RT35 with melting temperature at 35°C and thermal conductivity of 0.2 W/(m·K). Water was employed as heat transfer fluid with temperature difference between 15°C and 25°C compared with PCM. The results illustrated that the heat exchanger with PCM embedded in graphite matrix had normalized powers between 700-800 W/(m^2·K), which was 10 times larger than the others.

Rahimi et al. [19] employed the same PCM and heat transfer fluid in a fin-and-tube heat exchanger to study the impact of fins, fluid temperature and flow rate on the melting and solidification time. It was found that the solidification process was more sensible to the fin employment than the melting process while increasing fluid flow rate contributed more toward melting time.

Zhang et al. [20] integrated the paraffin wax as PCM into the air conditioning condenser to recover the heat for heating water. The melting temperature of the PCM was 45-48°C and the cooling capacity of the unit tested was 7,500 W. It took 60 minutes for the PCM to be fully melted and another 95 minutes to drop from 65°C to

45°C, which increased the water temperature from 25°C to 33.2°C at the flow rate of 100 L/h.

2.3 Closed Loop Thermosiphon

Thermosiphons are passive heat transfer devices without external power supply. Working fluid in a closed loop thermosiphon loop circulates by itself because of the pressure difference in different locations or assistance of gravity.

Dobriansky [21] summarized different types of natural convection loops as shown in Figure 1. Among these loops, (a)(c)(e) and (g) are closed loop thermosiphon with partition between the heat sink and heat source. (a) is single phase liquid thermosiphon loop, the pressure difference of working liquid at heat sink and heat source is the driving force for the self-acting loop. (c) is defined by the author as thermosiphon with a bubble lift, which accelerates the circulation in the two-phase thermosiphon. (e) is referred as closed loop two-phase thermosiphon (CLTPT). The working fluid absorbs heat from the heat source and vaporizes so vapor phase is the heat-carrier in the circulation. It releases the heat at the heat sink, condenses and flows down with assistant of gravity to complete the circulation. The vapor rises spontaneously due to the pressure difference of the saturation vapor at the heat sink and heat source. Compared with (e), (g) has a partition between vapor and liquid phase because of porous filling or small grooves on the inner surface.

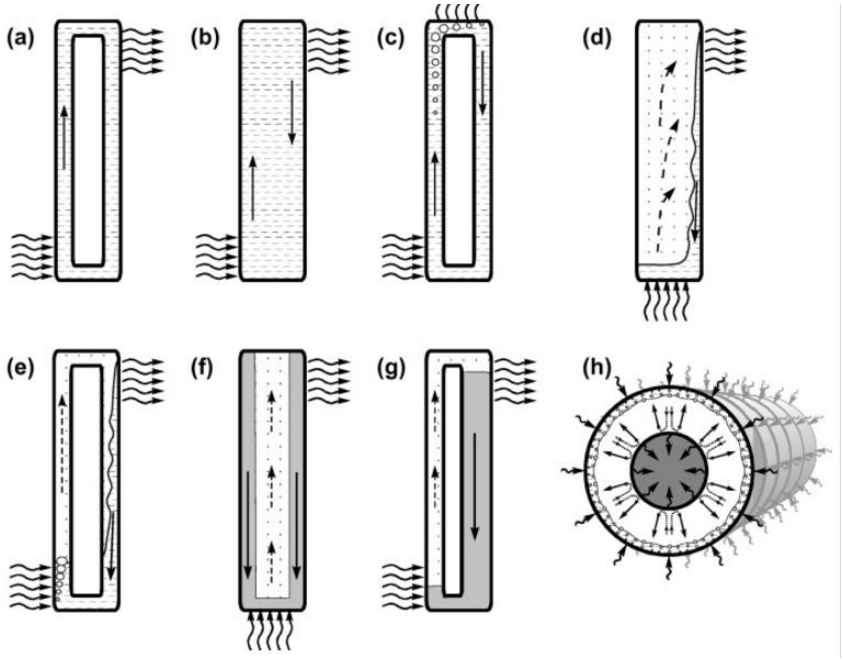

Figure 1: Diagrams of major natural convection loops [21]

The engineering applications employing thermosiphon loops include solar water heaters, geothermal systems, emergency cooling systems in nuclear reactors, electrical machine rotor cooling and electronic device cooling [22]. The research work of closed loop thermosiphon with R-134a as refrigerant is discussed in this section.

Abou-Ziyan et al. [23] studied the impact of vibration on the thermosiphon loop with 23 mm inner copper pipe diameter. The liquid filling ratio was 0.5 in the test. The vibration frequency varied from 0-3.33 Hz with input heat flux in a range of 160-380 kW/m^2. It was found that the normal working conditions without vibration was limited at 220 kW/m^2 heat input. At heat input higher than the limit value at 290 kW/m^2 or 380 kW/m^2, vibration increased the output heat flux up to 250%. It was also found in this study that vibration had less influence on R-134a than water as working fluid in the system.

Another experimental study conducted by Ong et al. [24] with R-134a in a 25.5 mm inner diameter copper tube thermosiphon evaluated the effects of temperature difference between heat sink and heat source, liquid filling ratio and mass flow rate on the system performance. The temperature difference varied from 0°C to 25°C, mass flow rate was in a range of 6.5 g/s to 12.1 g/s and filling ratio from 0.35 to 0.8. The results showed that the overall heat transfer coefficient increased with high mass flow rate, filling ratio and greater temperature difference between evaporating and condensing sections.

Thermosiphon loops with R-134a in small inner diameter tubes also draw attention of researchers in recent years. Khodabandeh et al. [25] investigated the influence of channel dimensions on two-phase thermosiphon loop. The evaporator of the thermosiphon was a small copper block with a rectangular channel milled in it. The width of the rectangular was around 5 mm with the height changed from 0.7 mm to 1.8 mm. For the small dimension of 0.7 mm and 0.9 mm, instability of flow was observed at low heat flux at 2 W/cm^2. The 0.7 mm channel had a maximum heat transfer coefficient of about 1.2 $W/cm^2 \cdot K$ at 10 W/cm^2 heat input. For channels with 1.3 mm, 1.6 mm and 1.8 mm inner diameters, they had similar performance with a maximum heat transfer coefficient of 2 $W/cm^2 \cdot K$ at 30-35 W/cm^2 heat input. This study demonstrated that larger inner tube diameters gave more stable system performance with higher heat transfer coefficient. Ong et al. [26] studied the two-phase flow pattern during macro-to-microchannel transition. The refrigerants include R-134a, R-234fa and R-245fa in small channels of 1.03 mm, 2.20 mm and 3.04 mm. Zhang et al. [27] investigated the partially liquid-filled downcomer on two-phase

thermosiphon loop with evaporator of 12 mm inner diameter. The distance between the evaporator and condenser varied from 0 to 1.5 m in this study. Other variables include the temperature difference between evaporator and condenser (0-36°C), refrigerant charge level (0.5-1.9 m) and circulation flow resistance opening (25-100%). The partially liquid-filled phenomenon was observed in the downcomer. It was also observed that the heat transfer rate increased approximately linearly with temperature difference except for lower charge at 0.5 and 0.7 m liquid level. Optimum refrigerant charges were also determined for different temperature difference cases.

Chapter 3: Experiment Setup

3.1 System Schematic

A schematic diagram of the system is shown in Figure 2. In the cooling mode, a vapor compression cycle was used (Figure 2 (a)). A 24 V lithium battery pack was used as a power supply to compressor, fan and control system of the portable platform. The condenser was placed inside a PCM container. When the system is running in the cooling mode, the condenser discharges the waste heat to the PCM and the PCM is melting gradually. When the RoCo stops working, it is electrically and thermally charged. During the charging process, the system was working as a gravity-assisted thermosiphon (Figure 2 (b)). In this mode, three ball valves in the system are open and the refrigerant bypasses from compressor, expansion valve and mass flow meter. The condenser in the vapor compression cycle serves as an evaporator in thermosiphon mode. Liquid refrigerant in the evaporator absorbs heat from the PCM and vaporizes. The vapor moves up along the vapor line and condenses in the air-cooled condenser. The condensed refrigerant flows down along the liquid line and completes the gravity-driven circulation. Since thermosiphon loop has high heat transport capability due to the refrigerant latent heat, it accelerates the solidification process of PCM as compared with natural convection. The refrigerant used in current system was R-134a.

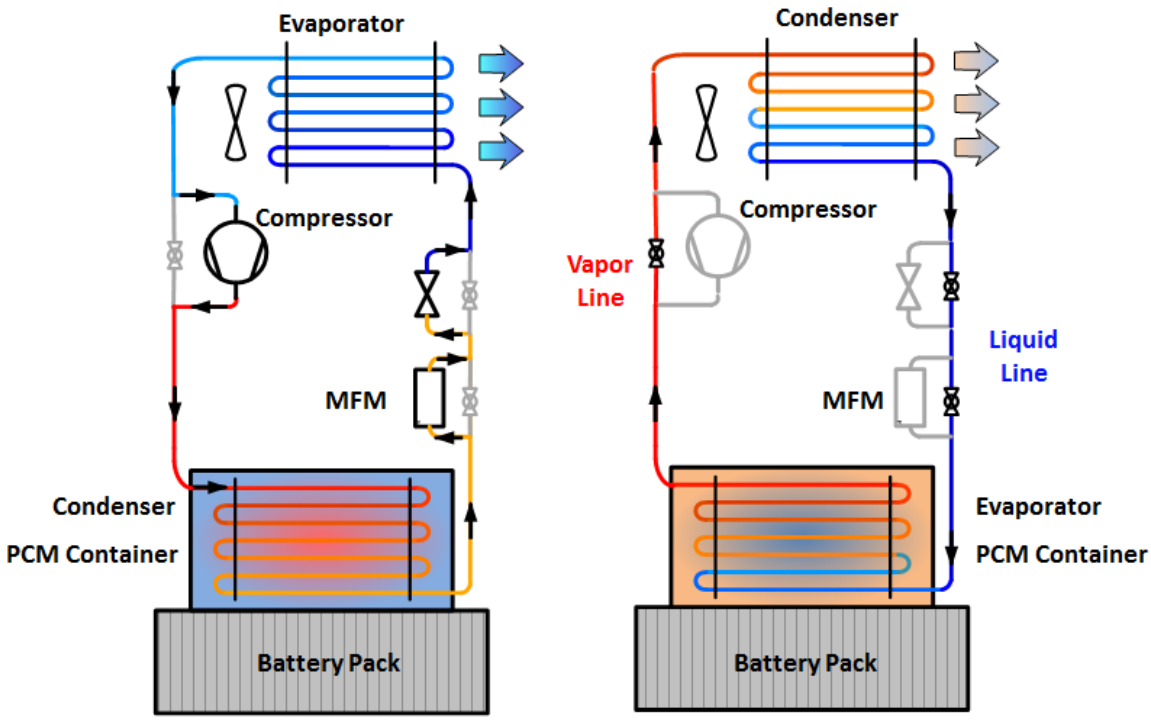

(a) vapor compression cycle (PCM melting process)

(b) thermosiphon system (PCM solidification process)

Figure 2: Schematic diagram of RoCo

3.2 Test Conditions and Procedures

The temperature setting in the room was assumed to be 26°C in the summer time, which was the chamber temperature. There were two types of tests conducted for the RoCo: one was the vapor compression cycle test, the other was the thermosiphon test. For the vapor compression cycle test, the PCM in the container was fully solidified before the beginning of the test. Three ball valves in the system were remained closed during the test. The compressor and fan were turned on when the test was started. System was operated continuously for about two hours until the PCM temperature indicated that it was fully melted. Thermosiphon test was followed after the vapor compression cycle test. In this mode, the compressor was turned off while the fan was

on during the test. Three ball valves were open manually. Thermocouples installed in the inlet and outlet of the condenser (working as an evaporator in the vapor compression cycle operation) recorded the airside temperatures. When the PCM in the container was observed to be fully solidified and the temperature difference between heat source and heat sink kept constant, the thermosiphon test finished.

3.3 Test Facility

In the RoCo system, the condenser heat exchanger integrated with PCM and the PCM container were designed and manufactured in the laboratory according to the performance requirements. Other components such as the battery pack, compressor, evaporator and fan were selected off-the-shelf and acquired from the market. Products specifications and design details are introduced in this section.

3.3.1 Battery Pack

RoCo is powered by lithium battery pack. A 3S7P battery pack with built-in protection circuit module from Shenzhen Masspower Electronic Co., Ltd was selected, shown in Figure 3.

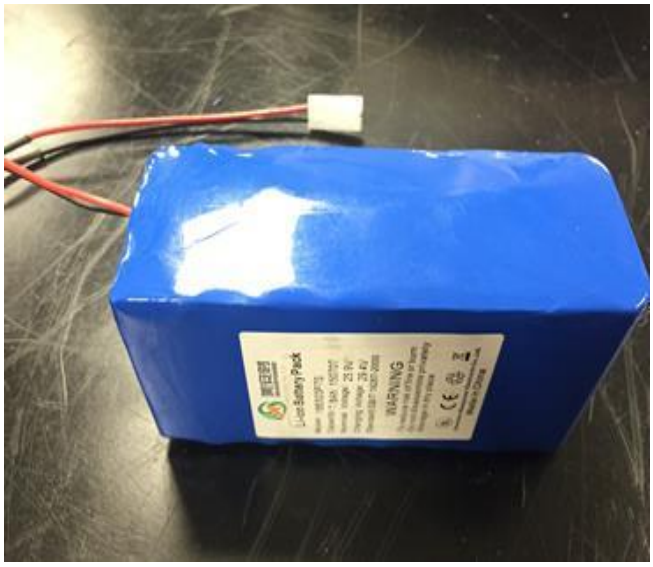

Figure 3: Battery pack from Masspower Electronic

The battery pack equipped with charging and discharging protectors and would automatically cut off when the voltage dropped under the lower limit. It has been tested before installed into the system. In order to evaluate the battery performance, the battery pack was fully charged first and connected to a 70 W fan since it was similar to the total power consumption of the RoCo. In this test, the battery discharge voltage was recorded as shown in Figure 4. The total running time was determined when the battery pack was automatically cut off. The voltage and capacity data were recorded in every 30 minutes in order to minimize interruptions. The battery pack ran for 175 minutes before cutting off, which was long enough for the RoCo to operate for two hours. Detailed voltage and energy discharged from battery pack are shown in Figure 4 and Figure 5, respectively. The battery pack specifics are in Table 1. The cut-off time in the test was longer than two hours and the change of voltage was smooth. Therefore, it was concluded that the system exhibited relatively reliable

performance since the battery pack provided a large enough voltage more than two hours.

Table 1: Product specifications and test details of Masspower battery pack

Variables	Unit	Value
Capacity	Ah	7.8
Nominal Voltage	V	25.9
Energy	Wh	202.2
Fully Charged Voltage	V	29.06
Cut-off Discharge Voltage	V	22.26
Running Time	min	175

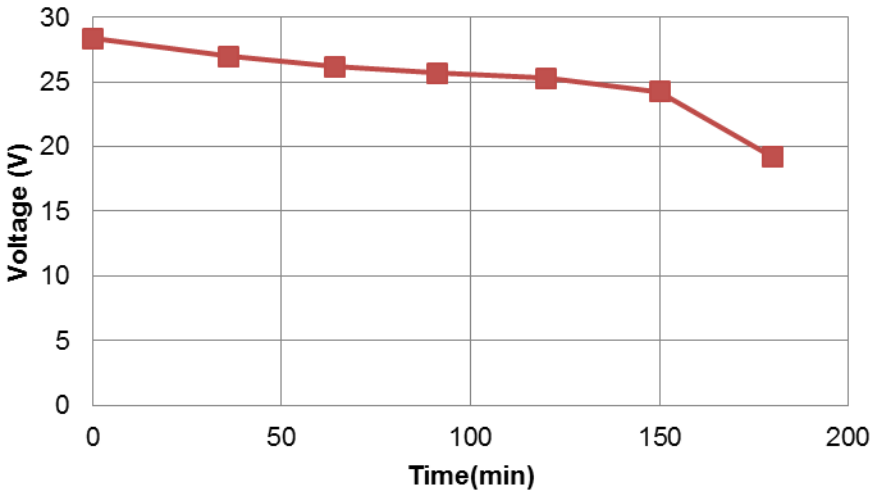

Figure 4: Discharge voltage variations when powered 70 W fan

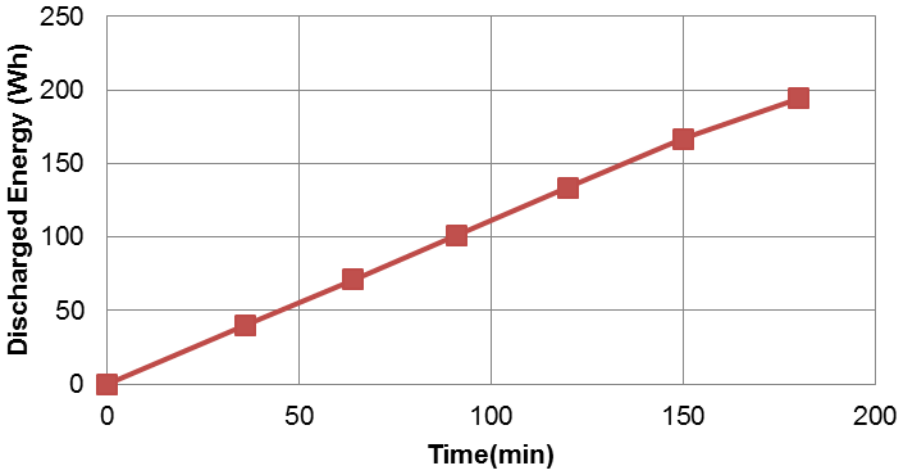

Figure 5: Discharged energy from battery packs

3.3.2 Compressor

The cooling capacity of the system was assumed to be around 100 W. An Aspen Q-serious rotary compressor was selected. It is a variable speed compressor with speed range between 2,100 – 6,500 RPM. It is working under 24 VDC and the displacement volume is 1.4 cc. The compressor comes with a high capacity drive. The operating voltage range for the board is between 20 – 30 V. The speed of the compressor is controlled by the voltage input from the drive. The compressor turns on with minimum voltage input of 0.8 volts and its speed increases linearly from 2,200 RPM to 6,500 RPM with voltage input from 0.8 volts to 4.5 volts. During the test, the input voltage was set constant at 0.8 volt and the compressor was operated at 2,200 RPM. Figure 6 shows the compressor and its drive.

Figure 6: Aspen compressor and high capacity drive

3.3.3 Evaporator and Fan

A model 720 copper tubes and copper fins heat exchanger from Thermatron was selected for the evaporator as shown in Figure 7. It has the corrosion protection both internally and externally. The joints were brazed with silver-solder. The original design of the evaporator is shown in left side of Figure 7. However, when the system works under the thermosiphon mode, the condensed refrigerant cannot flow through the tubes to the downcomer in this original design. Therefore, the circuitry of this evaporator was customized and the final design is shown in right side of Figure 7.

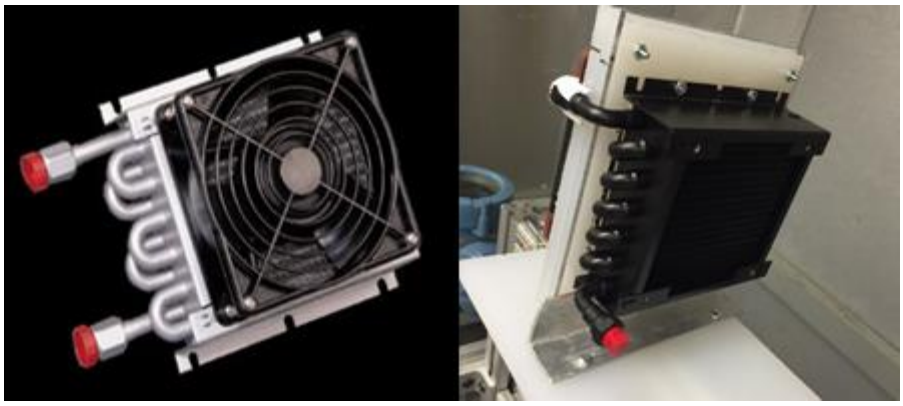

Figure 7: **Thermatron model 720 evaporator**

(Left: original design, right: customized design for thermosiphon mode)

The Thermatron evaporator came with a fan mounted to the frame of the evaporator. However, the fan motor is rated for 110 VAC power input. Therefore, it was replaced by the NF-A14 industrial PPC-3000 PWM fan by Noctua, as shown in Figure 8. It is rated for 12V and very quiet, with maximum noise level of 41.3 dbA at 3,000 RPM. The rated air flow rate is 158.5 CFM and the power consumption is 6.6 W.

Figure 8: Noctua NF-A14 PWM cooling fan

3.3.4 Condenser

A condenser was designed in four parallel spiral copper tubes as shown in Figure 9. Refrigerant flows down to the main tube at the top of the condenser, and assumed to be evenly distributed among these four branches. After the refrigerant condenses in the branches, it converges in the bottom main tube.

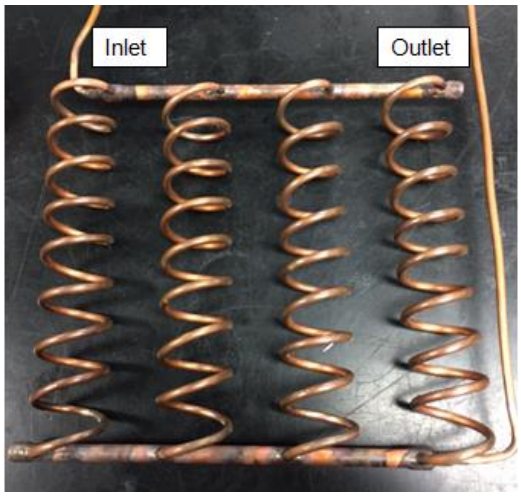

Figure 9: Spiral copper tube condenser

6.4 mm diameter tube was used to build the branches. Other system operating conditions are summarized in Table 2. For simplification, following assumptions were made for heat transfer and pressure drop analysis.

- The copper tube in the condenser was assumed to be straight to simplify the calculation although it was in spiral shape, but it. Under this assumption, the secondary flow due to centrifugal force was neglected.
- The refrigerant entered the condenser was assumed to be evenly distributed among four tubes. Therefore, each tube had the same heat transfer and pressure conditions.
- Copper tube wall temperature was assumed to be constant at 37.0°C, which was the melting temperature of PCM. The sensible heat of the PCM and temperature gradient along the tube were neglected.
- For the two-phase region, an average quality of 0.5 was used to calculate the heat transfer coefficient.

Table 2: System operating conditions for condenser design

Variables	Unit	Value
Condenser In Temp.	°C	60.0
Condenser In Pressure	kPa	1,262.0
Total Ref. Mass Flow Rate	g/s	1.0
Wall Temp.	°C	37.0
Condenser Out Temp.	°C	43.0

A summary of correlations used for heat transfer and pressure drop analysis is in Table 3.

Table 3: Summary of correlations for heat transfer and analysis

Correlation type	Heat Transfer	Pressure Drop
Refrigerant Liquid Phase	Gnielinski [28]	Blasius [29]
Refrigerant Two-phase	Shah [30]	Homogeneous [31]
Refrigerant Vapor Phase	Gnielinski [28]	Blasius [29]

For single phase heat transfer region, when Re number was larger than 2,300, which was the condition for vapor phase flow inside the tube based on the design operation conditions, Gnielinski equation [28] was used. It was the most practical formulation in predicting single phase heat transfer for turbulent flow [32]. The following equation was used to calculate the Nusselt number.

$$\mathrm{Nu}_{liq} = \frac{(f/8)(Re-1000)Pr}{1+12.7\left(\frac{f}{8}\right)^{\frac{1}{2}}(Pr^{\frac{2}{3}}-1)}[1+(\frac{D}{L})^{2/3}](\frac{\mathrm{Pr}}{Pr_w})^{0.11} \quad (1)$$

In equation (1), f was calculated out from Filonenko equation [33] below,

$$f = (1.82\lg(Re) - 1.64)^{-2} \quad (2)$$

When Re number was less than 2,300 in the liquid region, the following laminar flow heat transfer correlation [34] was used for the averaged Nusselt number calculation,

$$Nu_{vap} = 3.66 + \frac{0.065RePr\frac{D}{L}}{1 + 0.04(RePr\frac{D}{L})^{2/3}} \quad (3)$$

For the two-phase region, the mass flow rate was calculated to be 14.3 kg/m^{2}·s and Shah's correlations [30] were adopted for the heat transfer coefficient calculation.

$$h_{tp} = h_{LT}(\frac{\mu_f}{14\mu_g})^n[(1-x)^{0.8} + \frac{3.8x^{0.76}(1-x)^{0.04}}{Pr^{0.38}}] \quad (4)$$

Where

$$\mathrm{n} = 0.0058 + 0.557Pr \quad (5)$$

For the pressure drop analysis, Blasius equation was used for single phase region. Fanning factor f was calculated out based on the Re number.

$$\mathrm{f} = \frac{0.0791}{Re^{1/4}}, Re < 20000 \quad (6)$$

$$\mathrm{f} = \frac{0.046}{Re^{1/5}}, Re > 20000 \quad (7)$$

Based on the fanning factor, pressure loss can be calculated by the following equations,

$$\Delta\mathrm{p} = \rho\mathrm{g}\Delta\mathrm{h} \quad (8)$$

$$\frac{\Delta h}{L} = \frac{2fV^2}{gD} \quad (9)$$

In the two-phase region, a homogeneous pressure drop correlation was used.

Homogeneous void fraction could be determined from the quality, which was assumed to be constant at 0.5 in the calculation.

$$\varepsilon = \frac{1}{1 + (\frac{\mu_G}{\mu_L}\frac{1-x}{x}\frac{\rho_G}{\rho_L})} \tag{10}$$

Homogeneous density was obtained using following equation.

$$\rho = \rho_L(1-\epsilon) + \rho_G\epsilon \tag{11}$$

The static pressure drop for the homogeneous two-phase fluid was then calculated out.

$$\Delta p = \rho g \Delta h \tag{12}$$

A summary of the calculation results for one copper tube is shown in Table 4.

Table 4: Summary of heat transfer and pressure drop analysis for single tube

Region	Vapor	Two-phase	Liquid	Total
Length [m]	0.17	0.80	0.21	1.18
Capacity [W]	3.43	38.56	1.55	43.44
Pressure Drop [kPa]	0.14	1.00	0.02	1.16

3.3.5 PCM

In the test system, the condenser tubes were submerged in the PCM so that there was a direct heat transfer between refrigerant and PCM through tube wall. Therefore, PCM is a critical part of the system. The most important parameter to consider is the melting temperature of the PCM. Ideally, the melting temperature should be as low as possible since it leads to a lower condensing temperature and a higher system COP. However, at the same time, it should be higher than the possible highest indoor temperature so that it won't melt by itself when the system is not running. Besides,

the preferable product is with high heat storage capacity so that its weight is not too heavy. It should also have consistent performance over multiple thermal (melt/solidify) cycles and non-toxic. Based on those desired properties discussed above, PureTemp 37 from Entropy Solutions was selected to use in the system. It is a USDA Certified Bio based product. According to the technical data sheet by the manufacture, it was tested over a course of 10,000 cycles. The properties are summarized in Table 5.

Table 5: Properties of Pure Temp 37

Properties	Unit	Value
Melting Point	°C	37
Heat Storage Capacity	kJ/kg	210
Thermal Conductivity (liquid)	W/m·K	0.15
Thermal Conductivity (solid)	W/m·K	0.25
Density (liquid)	g/ml	0.84
Density (solid)	g/ml	0.92
Specific Heat (liquid)	J/g·K	2.63
Specific Heat (solid)	J/g·K	2.21

3.3.6 PCM Container

A PCM container was manufactured with PVC pipes as shown in Figure **10**. It was assumed that all of waste heat from condenser was absorbed in PCM and stored as latent heat. Considering the natural convection heat loss from the PCM to ambient, the safety factor of 1.4 was applied to the total mass of PCM needed. The PCM amount needed from estimation was 8.4 kg and the container could hold as much as 8.6 kg PCM, it is sufficient for two hours system running time. Figure 11 shows the condenser tubes fitted well inside the container.

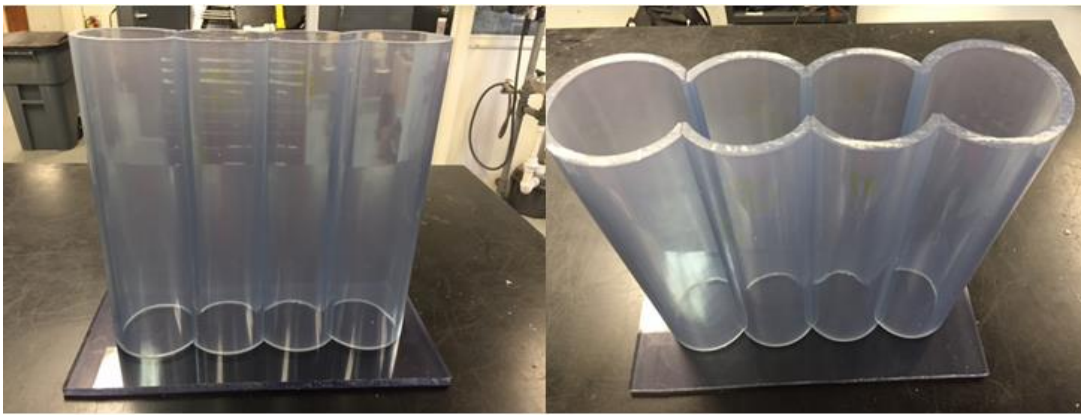

Figure 10: PCM containerTable 6: Design variables of the PCM container

Variable	Unit	Value
	VCC	
Condenser Capacity	W	174
System Running Time	hour	2
	PCM	
Latent Heat	kJ/kg	210
Density (liquid)	kg/m^3	840
Safety Factor	-	1.4
Total Amount Needed	kg	8.4
	Container	
Pipe I.D.	mm	97.2
Tube Height	mm	365.0
Total Volume	L	10.3
Maximum PCM Mass to contain	kg	8.6

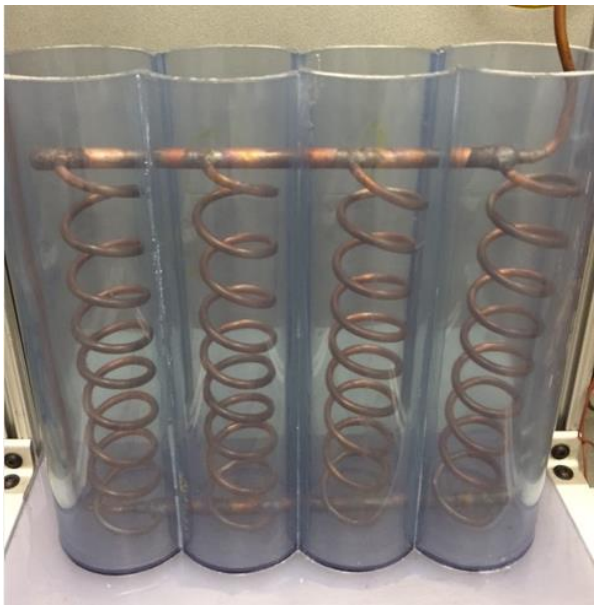

Figure 11: Condenser tubes inside PCM container

3.4 Instrumentation

Figure 12 shows actual system schematic with full instrumentation.

A receiver was installed in the liquid line of the system because the vapor compression cycle and thermosiphon loop had different charge requirements. For the thermosiphon to work, the evaporator (working as a condenser in vapor compression cycle) should be filled with refrigerant, or dry out would happen on the tube surface. To balance the charge difference between two modes, a 300 cc receiver was installed. When the RoCo first worked in the vapor compression cycle mode, a condensed liquid refrigerant from the condenser would accumulate gradually in the receiver until it reached a stable condition. When the system was switched to thermosiphon mode, the liquid refrigerant inside the receiver drained down into the evaporator and filled it. Then the system could work as a thermosiphon loop with adequate filling ratio.

A rubber piece was placed on the bottom of the condenser so that in the thermosiphon mode, the bubbles generated in the evaporator would not be trapped. The tubes connecting to the mass flow meter and receiver were also designed to be inclined to control the flow by gravitation. The liquid refrigerant in the downcomer would not enter the mass flow meter and stay in it.

Two sight glasses were installed at the inlet and outlet of the condenser. In the vapor compression cycle, the sight glass at the outlet of the condenser helped properly charge the system. If bubbles were observed in the sight glass, then the refrigerant at the condenser outlet was not saturated or subcooled liquid, which indicated more charge was needed. In the thermosiphon mode, bubbles should exist in the sight glass at the outlet of the evaporator and down flowing liquid should be observed in the evaporator inlet, which demonstrated the refrigerant circulation in the thermosiphon loop.

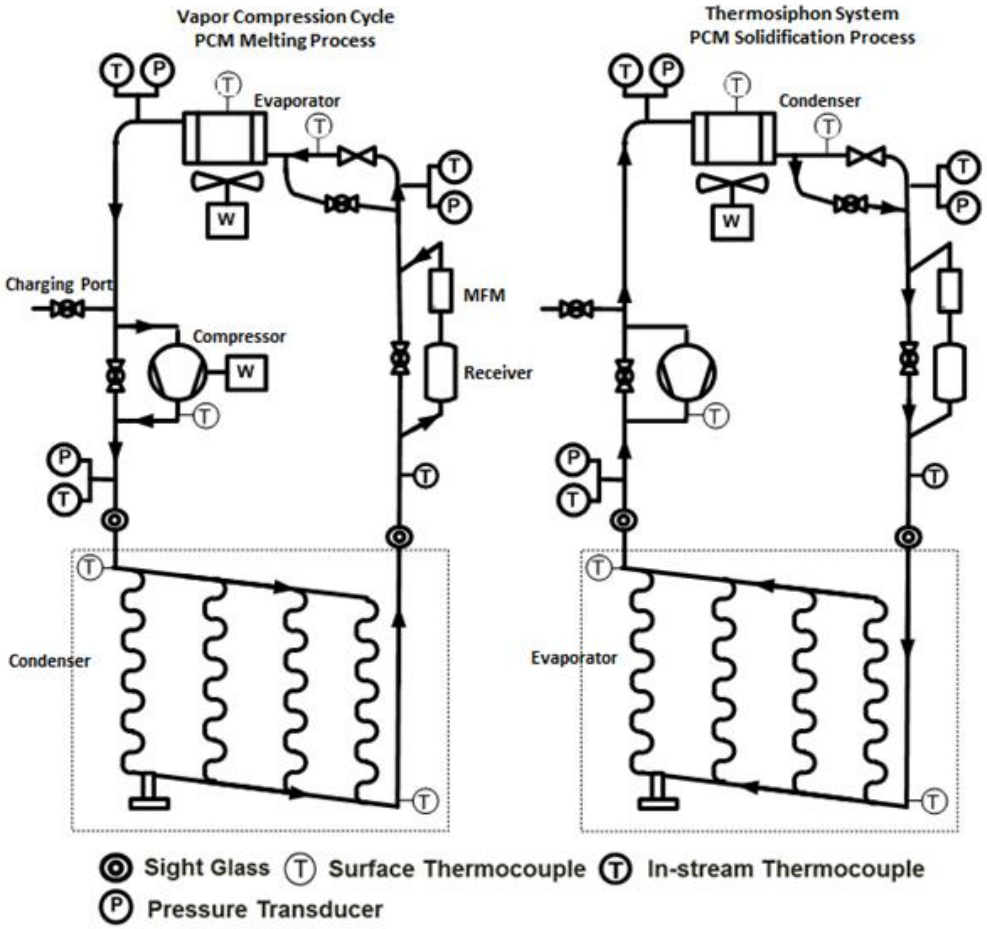

Figure 12: RoCo schematic with full instrumentation

3.4.1 Pressure Transducer

Pressure transducers were installed at the condenser outlet, evaporator inlet and expansion valve inlet as shown in Figure 13. Two of them were absolute pressure transducers from Setra, which were installed at the expansion valve inlet and evaporator outlet. They were strain pressure transducers in the range of 0-500 PSIA. One of them was gauge pressure transmitter manufactured by WIKA, the range of which was 0-500 PSIG. It was at the compressor discharge. The standard atmospheric pressure was assumed to be 101.325 kPa in the test chamber and it was added to the measured pressure value of the gauge pressure transmitter in LabVIEW. Therefore,

the pressure data recorded were all in absolute pressure value. Specifications of the pressure transducers are summarized together with other instruments in summary section.

Figure 13: Pressure transducers installed in system (Left: Setra pressure transducer at evaporator outlet; middle: Setra pressure transducer at expansion valve inlet; right: Omega pressure transmitter at compressor discharge)

3.4.2 Thermocouple

Both in-stream and surface thermocouples were used to measure temperatures in the refrigerant side. Considering that the temperature range in the test was between 0-80 °C, T Type thermocouples were used for the temperature measurement. All of the thermocouples used were calibrated between 0-80°C, with 10°C temperature increment at each point. The uncertainty of temperature measurement was 0.5°C. There were two types of T Type thermocouples, as shown in Figure 14. One was the surface thermocouple attached to the copper tube to measure the surface temperature of the refrigerant tube, or installed in the air and PCM to measure the temperature.

The other was the in-stream thermocouple to be inserted to the refrigerant stream to measure the in-stream temperature.

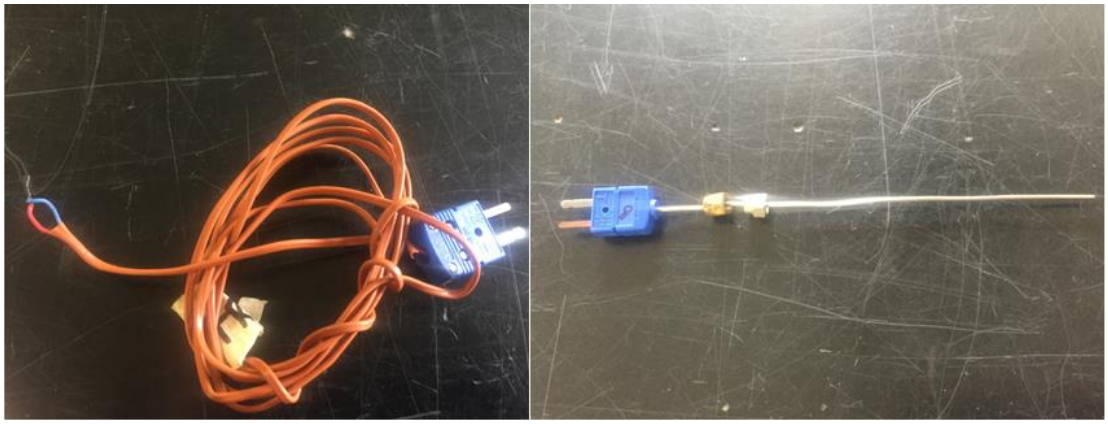

Figure 14: T type thermocouples

(Left: surface thermocouple, Right: in-stream thermocouple)

In the refrigerant side, both surface and in-stream thermocouples were used. The locations of those thermocouples were shown in

Figure **15**. There were two in-stream thermocouples before and after the receiver and mass flow meter in the liquid line since they were sources of heat loss. From the temperature measurement for these two locations (number 1 and number 2 thermocouples in

Figure **15**), heat loss was calculated. The refrigerant with highest temperature was at compressor discharge, which was another major source of heat loss from the system. Therefore, the surface thermocouple installed (number 7 in

Figure **15**) helped determine the heat loss from compressor discharge to condenser inlet. Pictures of those thermocouples in the system set up are shown in

Figure **16** and Figure 17. Surface thermocouples were attached to the copper tubes and zip tied with insulation foam.

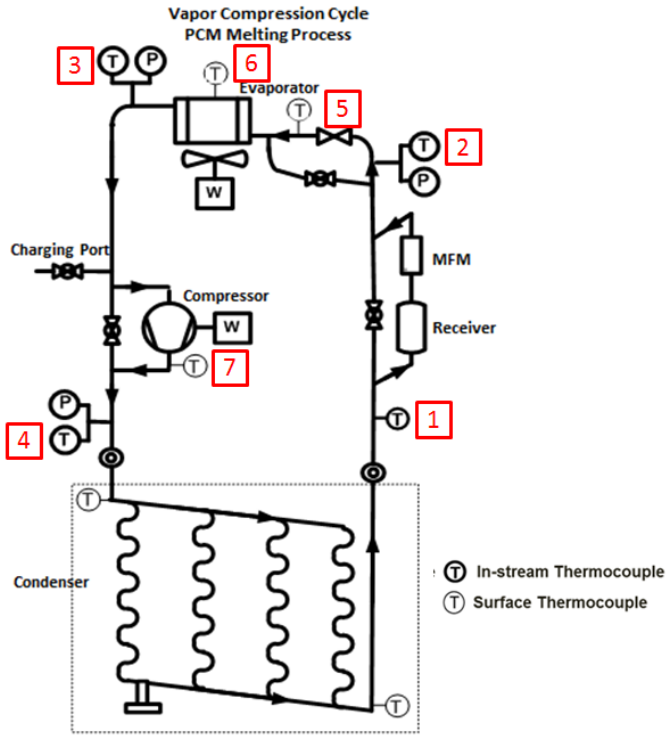

Figure 15: Refrigerant side thermocouple locations

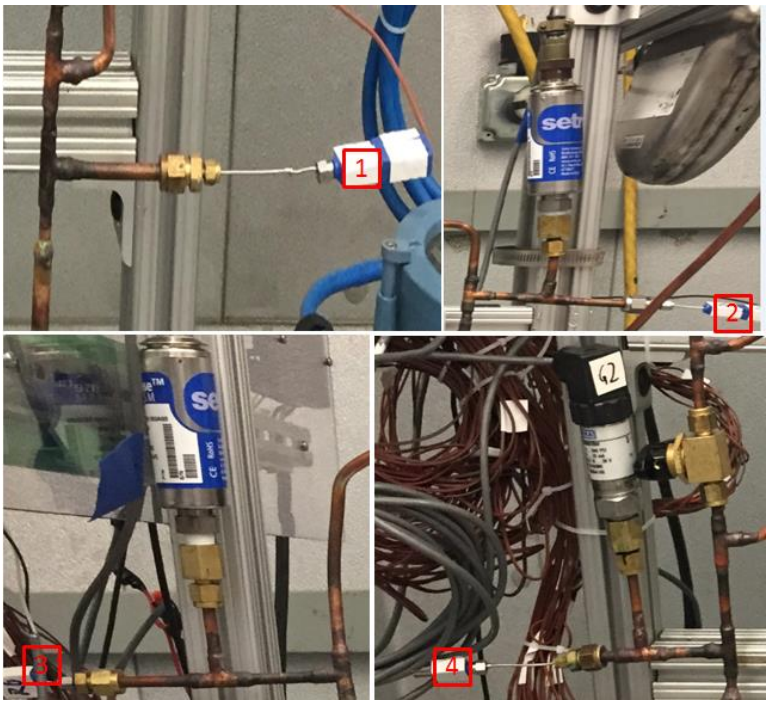

Figure 16: Refrigerant side in-stream thermocouple locations

Figure 17: Refrigerant side surface thermocouple locations

Surface thermocouples were installed to the inlet and outlet of the evaporator to measure the airside temperatures. Since the fan and the evaporator were mounted together to minimize the airside pressure drop, the thermocouples were attached to the fan frame to measure the evaporator outlet air temperature.

Figure 18: Airside thermocouple locations

(Left: evaporator inlet; Right: evaporator outlet)

Thermocouples were also installed on the condenser surface and different locations inside the PCM container to measure the temperature profile during the PCM melting and solidification processes.

Figure 19 shows the locations of all the thermocouples installed inside the PCM container. In Figure 19, numbers in red indicated the surface TCs while those in yellow were merged in PCM either to measure the inner temperature or close-to-wall outer temperature. There were three different planes to place the thermocouples: bottom plane (see TC 1,TC2,TC3,TC10,TC11,TC12,TC21,TC24 in Figure 19), middle plane(see TC4,TC5,TC6,TC13,TC14,TC15,TC20,TC23 in Figure 19) and upper plane(see TC7,TC8,TC9,TC16,TC17,TC18,TC19,TC22 in Figure 19). On the left and right spiral tubes of the condenser, there were three thermocouples placed on the same plane, Figure 20 shows the details of how they were installed. The inner TC was in the middle of the spiral tube while the outer TC measured the PCM temperature close to the container. Surface TC was attached directly to the copper tube. On the middle two spiral tubes, three surface TCs were attached to each column.

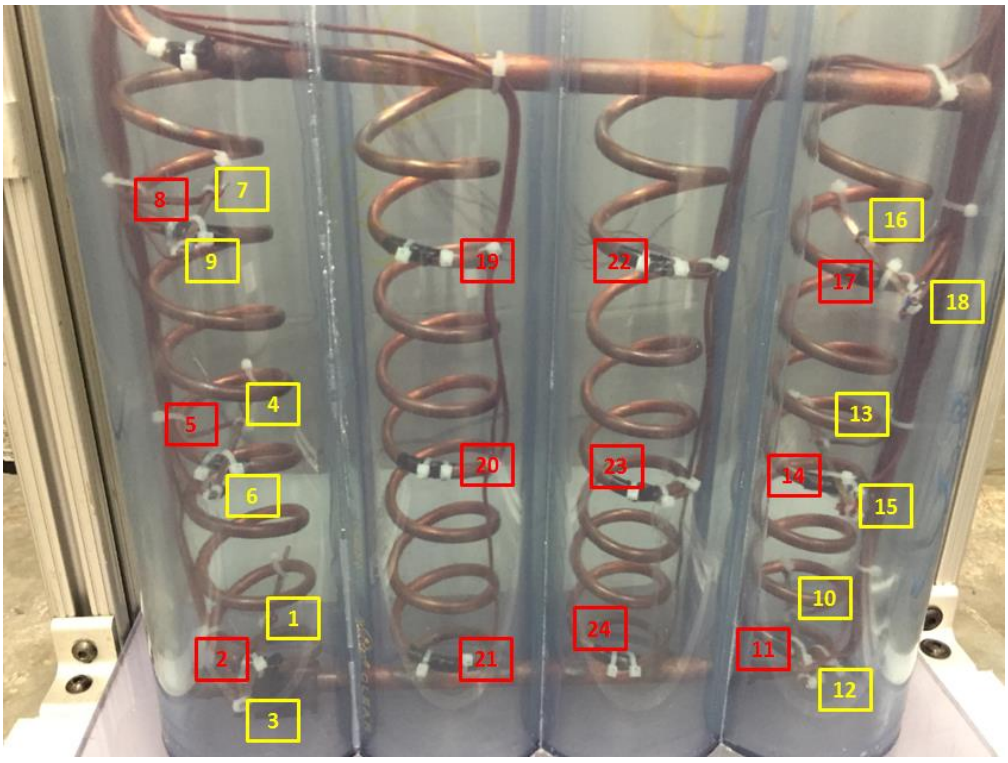

Figure 19: Thermocouple locations inside the PCM container

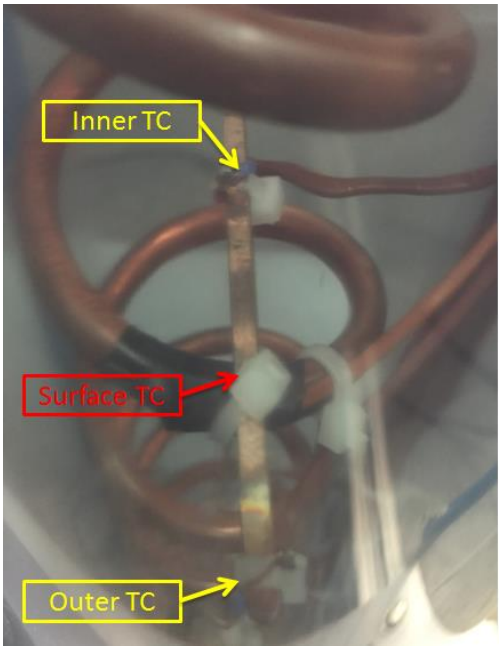

Figure 20: Thermocouple locations on the same plane inside the PCM container

3.4.3 Mass Flow Meter

The estimated refrigerant mass flow rate in the system was 1 g/s, so the Micro Motion Coriolis flow meter was used in the system. The mass flow meter was installed in the liquid line of the system, since it had higher measurement accuracy on higher density (±0.25% of rate for gas and ±0.10% of the rate for liquid). The mass flow meter was calibrated in a range of 0 – 3 g/s before installation into the system. Micro Motion Model 2700 transmitter was connected to the mass flow meter to output the flow rate measured. The mass flow meter and the transmitter are shown in Figure 21.

Figure 21: Mass flow meter and the transmitter

3.4.5 Power Meter

Power meter by RC Electronics, Inc. was used to measure the power consumption of the system. It was connected to a battery pack and measured current (Amps), voltage (Volts), power (Watt), energy (Watt-hours) and charge (Amp-hours) values in real-time and displayed all those variables alternately. It was connected to a 24V auxiliary battery during the test. Therefore, the power consumption of the meter itself would not influence the measured values. The picture of power meter is shown in Figure 22.

Figure 22: Watt meter

Before the system was tested with battery pack as a power supply, it was operated with an external 24 VDC power supply. To measure the power consumption from the compressor and fan, the compressor and fan wires were circuited through the DC current and voltage transducers, shown in Figure 23.

Figure 23: DC current and voltage transducers

3.4.6 Summary

Table 7 shows specifications of instrumentation used in the system. The experiment setup with full instrumentation is shown in Figure 24. The total height of the setup was around 0.9 m.

Table 7: Specification of instrumentations

Instrument	Type	Manufacturer	Model	Range	Systematic uncertainty
Pressure Transducer	Strain	Setra	AccuSense™ Model ASM	0-500 psia	±0.05% span
Pressure Transducer	Strain	WIKA	S-10	0-500 psig	±0.25% span
In-stream TC	T-type	Omega	TMQSS062G6	(-250)-350°C	±0.5°C
Mass Flow Meter	Coriolis	Micro Motion	CMFS010M	0-3 g/s (calibrated)	±0.10% reading
Watt Meter	Watt transducer	RC Electronics	Watt's Up	0-6,554W	±0.1W
DC Current Transducer	Hall effect	CR Magnetics	CR5211-10	0-10 ADC	±1.0%
DC Voltage Transducer	-	CR Magnetics	CR5310-50	0-50 VDC	±1.0%

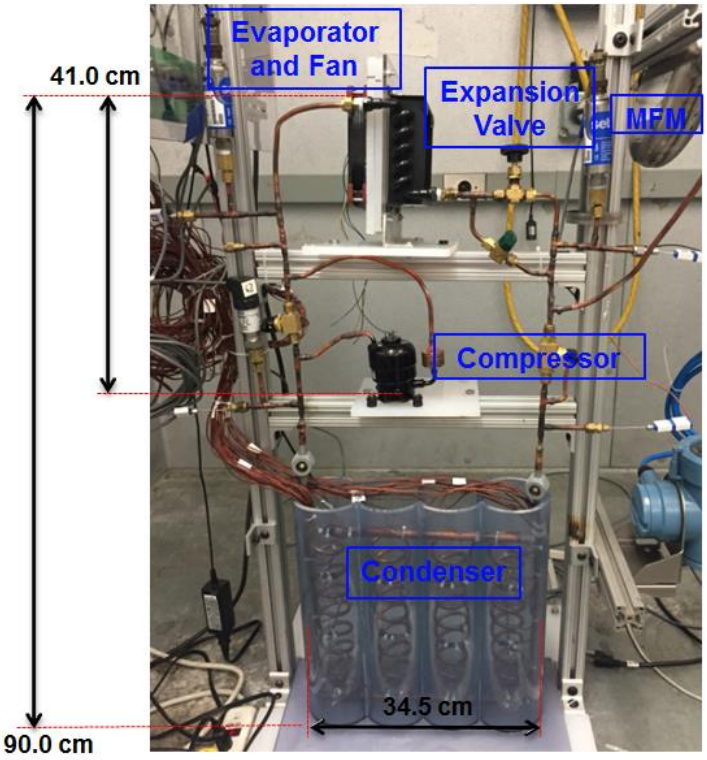

Figure 24: Experiment setup

3.5 Data Acquisition System

Six DAQ modules from National Instruments, shown in Figure 25, were installed to read to signal outputs from the instrument to the LabVIEW program. Three of them were module NI9214 for thermocouples. One was NI9207 for measuring ±10 V and ±20 mA analog outputs from pressure transducers, mass flow meter, DC current transducers and DC voltage transducers. NI9472 24V sourcing digital output was used to power the instruments. NI9265 20 mA analog output was used to provide a 0.8 volt speed control signal for the compressor.

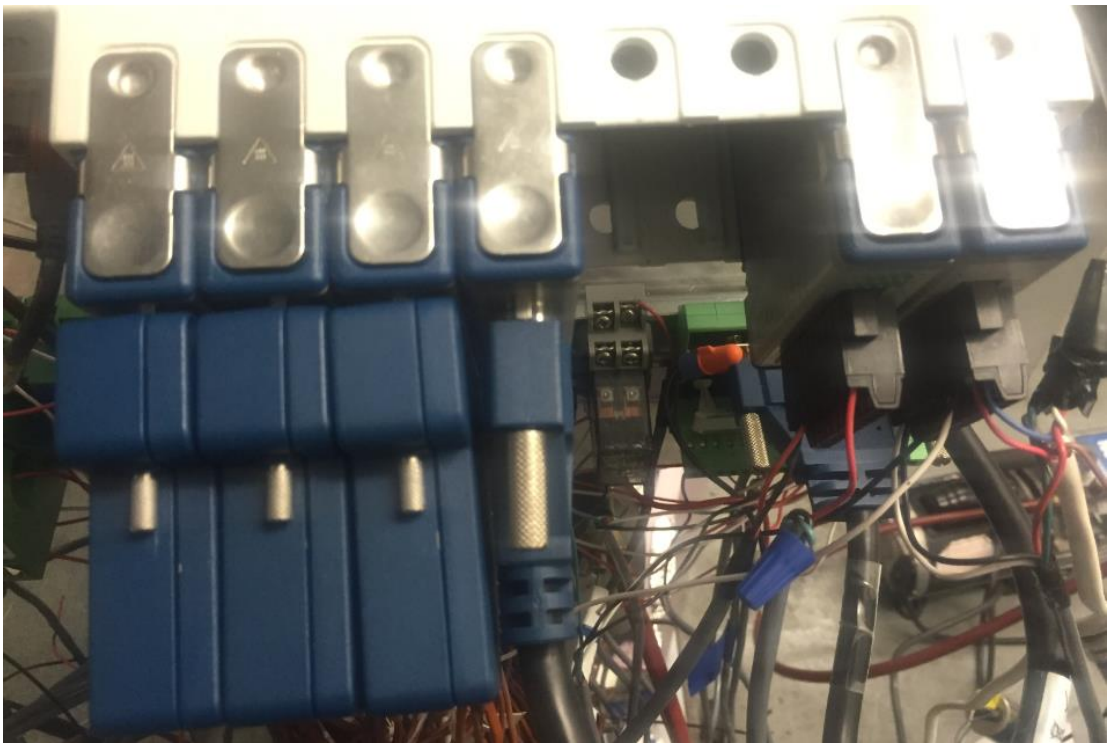

Figure 25: NI DAQ modules

3.6 Uncertainty Analysis

When conducting experiment and analyzing the data acquired, uncertainty analysis on the data collected is important for proper data evaluation. Uncertainty refers to the errors in measurement from the instruments utilized. The total uncertainty of a parameter measured consists of two parts: systematic uncertainty and random uncertainty. There are many factors contributing to the systematic uncertainty, like the quality and accuracy of the instruments, minor changes in the testing environment and inaccuracy of observation. Systematic uncertainties can be constant (T Type thermocouples), functional of scale (pressure transducers) or functional of measured value (mass flow meter). To reduce the system uncertainty in the current system, pressure transducers, thermocouples and mass flow meter were carefully calibrated in

the test range. Random uncertainty is due to random variations and is estimated by a standard deviation (STD).

In this experiment setup, directly measured data include: temperature, pressure, mass flow rate, and power consumption. Based on the directly measured variables, parameters like superheat, subcool, enthalpy, capacity and COP can be calculated accordingly.

Total uncertainty of measured parameters can be determined by

$$\omega_{\text{total}} = \omega_{\text{sys}} + \omega_{\text{rand}} \tag{13}$$

Total uncertainty of calculated parameters can be determined by error propagation

$$\omega_{\text{f}} = \sqrt{(\frac{\partial \text{f}}{\partial \text{x}_1}\omega_{\text{x}_1})^2 + (\frac{\partial \text{f}}{\partial \text{x}_1}\omega_{\text{x}_1})^2 + \cdots + (\frac{\partial \text{f}}{\partial \text{x}_\text{n}}\omega_{\text{x}_\text{n}})^2} \tag{14}$$

Where

$f = calculated\ parameter$

$\omega_f = total\ uncertianty\ of\ calculated\ parameter\ f$

$x_i = measured\ parameter$

$\omega_{x_1} = total\ uncertainty\ of\ measured\ parameter$

$n = number\ of\ variables\ used\ to\ calculate\ f$

In the test, the heat from the condenser was directed into the PCM and PCM melted gradually. It was a dynamic and transient process, since the melting of PCM resulted in the loss of capacity of the condenser and further reduced the system performance. Therefore, only the system uncertainty was considered here. Table 8 summarizes the

systematic uncertainties in the system. Directly measured parameter values were from the test measurement.

Table 8: Calculation of systematic uncertainties

Variables	Unit	Value	Systematic uncertainty
Refrigerant Side			
Comp. Discharge Pressure	kPa	1,336.8	8.6
Cond. Out Pressure	kPa	1,330.5	1.7
Evap. Out Pressure	kPa	481.3	1.7
Expansion Valve In Temp.	°C	35.5	0.5
Cond. Out Temp.	°C	41.8	0.5
Comp. Discharge Temp.	°C	61.7	0.5
Evap. Out Temp.	°C	22.5	0.5
Mass Flow Rate	g/s	1.00	0.001
Compressor Power	W	54.7	0.8
Fan Power	W	3.5	0.05
Superheat	K	8.0	0.5
Subcool	K	8.6	0.5
Evap. Capacity	W	165.5	0.9
Cond. Capacity	W	178.7	1.0
System COP	-	2.83	0.04
Air Side			
Avg. Evap. Inlet Temp.	°C	26.3	0.25
Avg. Evap Outlet Temp.	°C	22.7	0.25
Evap. Capacity	W	172.8	16.8

Chapter 4: Test Results

4.1 Baseline Vapor Compression Cycle

Before the baseline test, the PCM was melted and poured into the condenser container, as shown in Figure 26. Chamber temperature was then set to be 26°C until the PCM was fully solidified. Then both the PCM container and the copper tubes in the system were insulated.

Figure 26: Liquid phase PCM inside condenser container

4.1.1 Charge Optimization

Charge optimization tests were first conducted to determine the charge with highest system COP. Tests were conducted with charge amount of 439 g, 455 g and 484 g for two hours. The case with 439 g was the minimum charge into the system when no bubbles were observed from the condenser outlet sight glass, which indicated there was subcooled liquid at the outlet of the condenser. In the test period, the expansion

valve was manually regulated so that the superheat maintained in a range of 5 – 8 K. The averaged variable values for each test during stabilized period were summarized in Table 9. The uncertainty values varied a little bit in different charges because of the measured values varied. The numbers in this table were for the uncertainty calculation results from 455 g charge.

With the increasing charge, both suction and discharge line pressures increased. The mass flow rate didn't change much because the addition of less than 20 g charge was a relatively small portion compared with 439 g minimum charge. The compressor did more work because of the increased mass flow rate, which resulted in an increase of power consumption from 55.1 W to 58.5 W. In the meantime, the cooling capacity improved from 160.6 W to 167.2 W while the system COP had an optimum value at 2.85 under the charge amount of 455 g.

Figure 27 and Figure 28 show suction and discharge pressures, evaporator capacity and system COP under different charge amounts. Error bars were also shown in Figure 27. But compared with the absolute pressure value, the uncertainties were trivial and hardly can be seen from the Figure 27.

From the charge optimization tests, the case with 455 g charge was concluded to be the optimum case among the three. The following sections discuss the detailed system performance with 455 g charge.

Table 9: Charge comparison

Variable	Unit	439 g Charge	455 g Charge	484 g Charge	Absolute Uncertainty
Suction Pressure	kPa	478.5	481.3	491.9	1.7
Discharge Pressure	kPa	1,318.2	1,336.8	1,418.7	8.6
Evaporating Temp.	°C	14.4	14.5	15.2	0.1
Condensing Temp.	°C	50.0	50.5	52.9	0.3
Mass Flow Rate	g/s	1.00	1.00	1.01	0.002
Superheat	K	8.0	8.0	5.7	0.5
Subcool	K	3.2	7.4	13.6	0.5
Comp. Power	W	55.1	54.7	58.5	0.8
Evap. Capacity	W	160.6	165.6	167.2	0.9
System COP	-	2.74	2.85	2.70	0.04

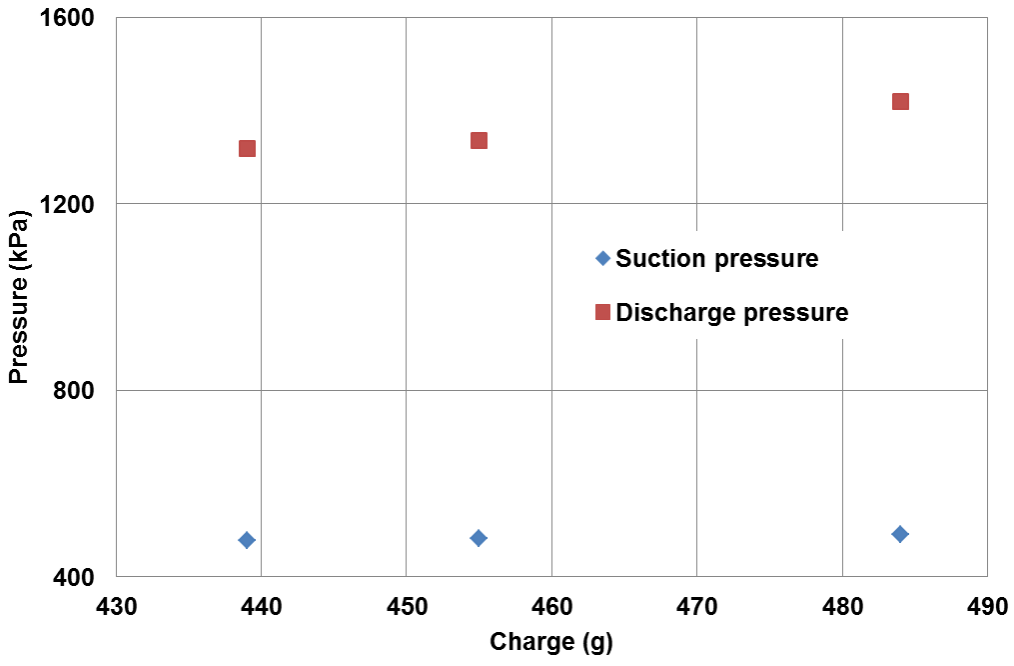

Figure 27: Operating pressures under different refrigerant charge amounts

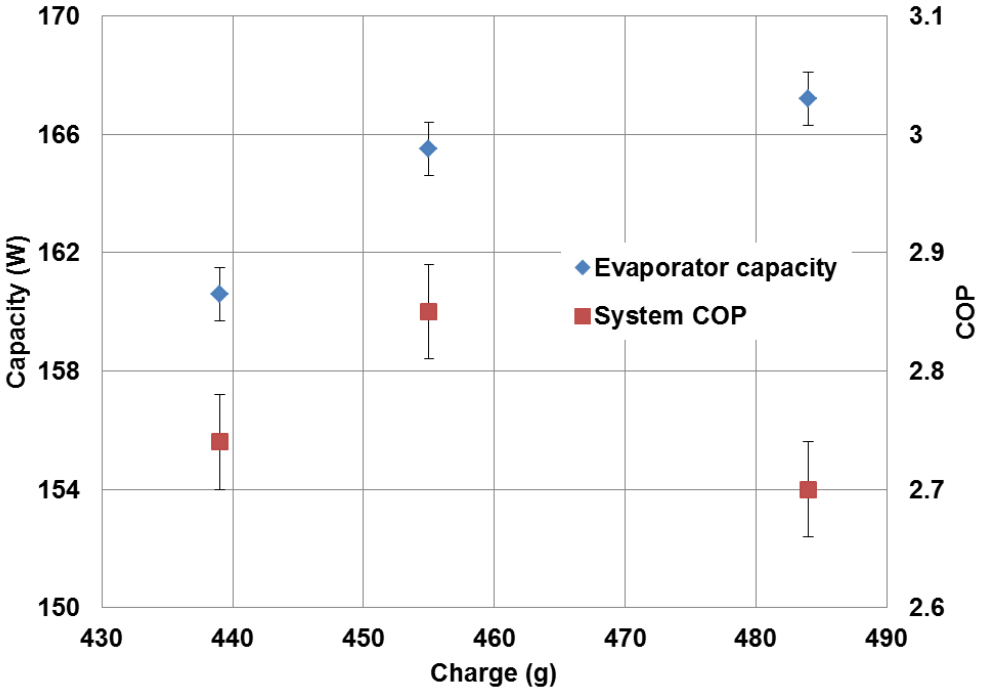

Figure 28: Evaporator capacity and COP under different refrigerant charge amounts

4.1.2 Repeatability Test

To ensure that the test results were reliable, a repeat test was conducted for 455 g charge case. The PCM was solidified under 26°C temperature setting. The refrigerant from previous test was recovered and the system was evacuated. The pure R-134a was then charged into the system until it reached 455 g charge. Same test process was repeated. In these two tests, data in the stable period from 40 minutes to 80 minutes was summarized in Table 10, which shows a high repeatability of the test.

Table 10: Repeat test under 455 g refrigerant charge

Variable	Unit	1st test	2nd test	Difference (%)
Suction Pressure	kPa	481.3	482.4	0.2
Discharge Pressure	kPa	1,336.8	1,353.0	1.2
Evaporating Temp.	°C	14.5	14.6	-3.9
Condensing Temp.	°C	50.5	51.0	1.0
Mass Flow Rate	g/s	1.00	1.01	1.0
Superheat	K	8.0	7.4	-7.5
Subcool	K	7.4	7.4	0
Comp. Power	W	54.7	54.2	-0.9
Evap. Capacity	W	165.6	164.1	-0.9
System COP	-	2.85	2.85	0

4.1.2 System Performance

In this section, test results under 455 g refrigerant charge are discussed in details.

Refrigerant side

Figure 29 shows the refrigerant side pressure change during the whole test period and Figure 30 provides the temperature details in different status of the system. The first test with 255 g ran for more than two hours to observe when the PCM was fully melted. From both pressure and temperature figures, there was a long start-up period about 25 minute before the system stepped into a relatively stable status. This is due to the 300 cc receiver installed in the liquid line. When the compressor started, the refrigerant would fill the receiver first. During the test period, the superheat did not maintain at a stable value by itself. Therefore, the expansion valve was manually regulated to keep it in the range of 5 – 8 K. The regulation operations resulted in the minor fluctuations in temperatures and pressures.

After 90 minutes from the start, the compressor discharge pressure and temperature began to increase. This is because the PCM was partly melted at the time so that condensing pressure was increased. The readings from the thermocouples installed into the PCM container were all above the melting temperature of PCM (37°C), at 121 minutes. It indicated that the PCM was fully melted, which demonstrated that the system satisfied the requirement of two hours continuous running time.

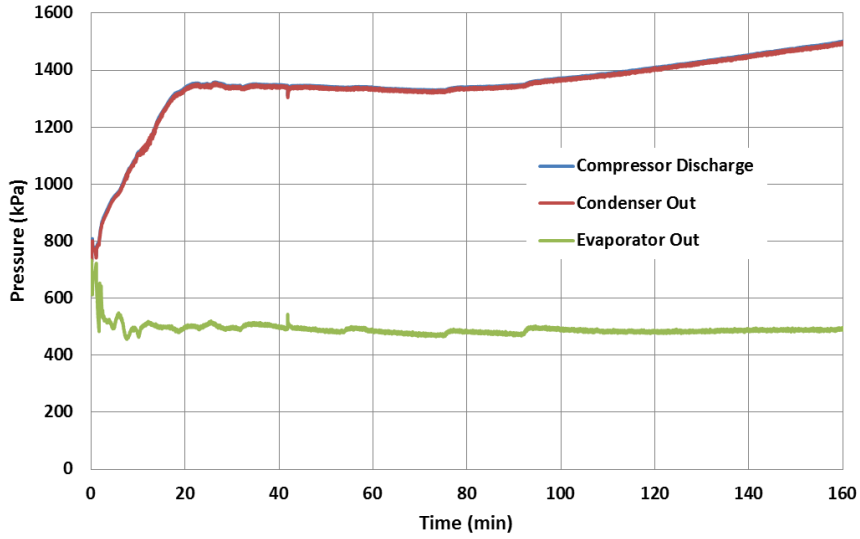

Figure 29: Refrigerant side pressure during vapor compression cycle test

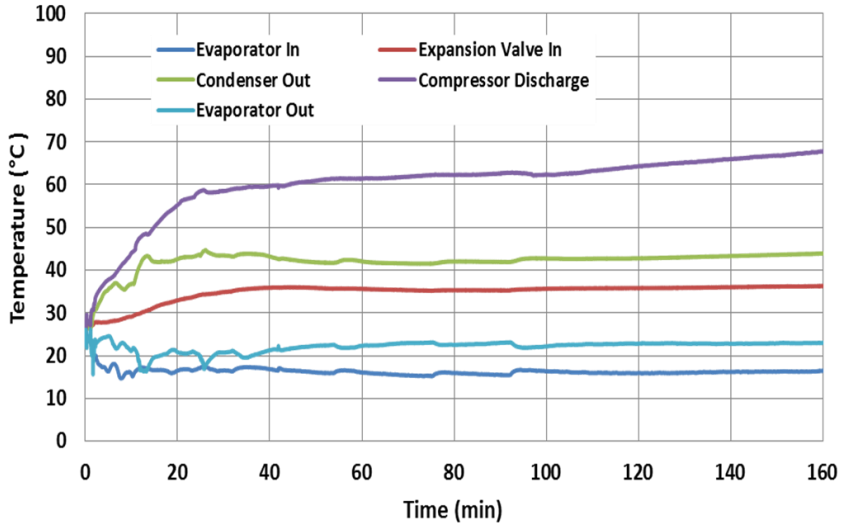

Figure 30: Refrigerant side temperature during vapor compression cycle test

Test data from 50 minutes to 80 minutes during the stabilization period was averaged and summarized in Table 9. The results were discussed in section Charge Optimization.

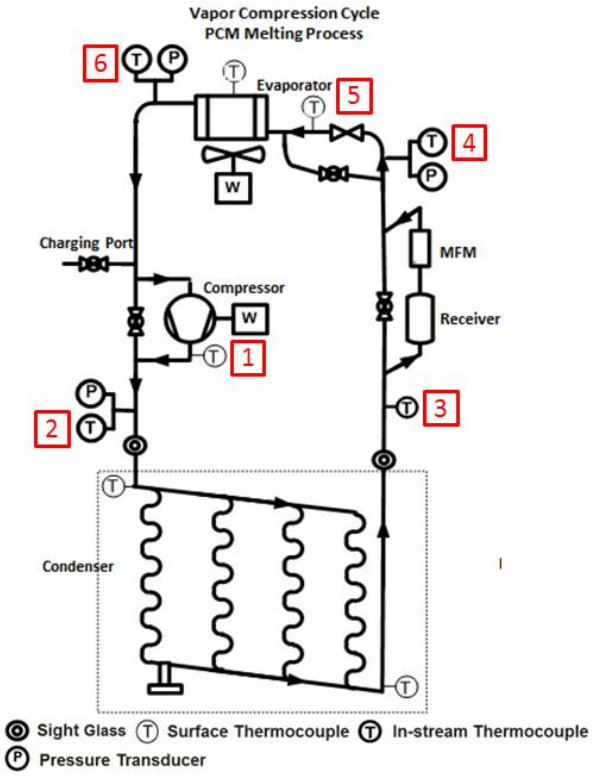

Figure 31: Positions of each status point

Table 11: Refrigerant properties at different state point

State Point	Pressure (kPa)	Temperature (°C)	Enthalpy (kJ/kg)
1: Comp. Discharge I	1,336.8	64.8	440.5
2: Comp. Discharge II	1,336.8	61.7	437.0
3: Cond. Out	1,330.6	41.8	259.1
4: Expansion Valve In	1,330.6	35.5	249.7
5: Evap. In	501.6	15.8	249.7
6: Comp. Suction	481.3	22.5	414.5

Table 11 summarizes refrigerant properties at different state points in the system. Several assumptions were made on the vapor compression cycle: first, the refrigerant in the expansion valve underwent an isenthalpic process (same enthalpy for state 4 and 5); second, there was no pressure drop along the mass flow meter and receiver (same pressure for state 3 and 4); third, there was no pressure drop from state 1 to state 2. State 1 and state 2 were listed separately, because the refrigerant was at higher temperature at compressor discharge. It helped determine the heat loss of the system. The measured evaporator inlet temperature was 15.8°C, which was based on a surface thermocouple measurement. The real refrigerant temperature should be lower than this value because of factors like poor contact and heat loss.

The quality at the evaporator inlet was 0.15. The condensing temperature of the condenser was 50.5°C, which was quite high. It was mainly due to the heat transfer limit in the PCM: the thermal conductivity was only 0.15 W/m·K for liquid phase and 0.25 W/m·K for solid phase. To decrease the condensing temperature and further improve the system performance, heat transfer enhancement should be made between the condenser tube and PCM. Options include adding fins to the heat exchanger to enlarge the contact surface area, or using graphite foam as a substrate to improve the PCM thermal conductivity [35].

Compressor performance was also evaluated by the test data. The measured temperature from state point 1: comp. discharge I was used to calculate to isentropic efficiency. The calculated isentropic efficiency and volumetric efficiency were 85% and 87%, respectively. An independent study on the same model Aspen compressor [36] showed that when the speed was in a range of 3,000-6,000 RPM, the volumetric

efficiency varied from 73.2% to 90.5% while isentropic efficiency was between 44.1% and 70.3%. The relatively high estimation of the isentropic efficiency may result from the inaccurate measurement of compressor discharge temperature. It was measured by a surface thermocouple instead of an in-stream one, which measured lower temperature than it actually should be.

Air side

From the measurement of the inlet and outlet of the evaporator, air side temperature change was known. Fan power consumption was used to calculate the air flow rate of the fan. Then the air side evaporator capacity was calculated.

The geometric information of the evaporator and the air side and refrigerant side operating conditions were provided to the CoilDesigner [37] to model the evaporator performance. Table 12 lists the correlations used in the model.

Table 12: Correlations used for the evaporator model

Correlation Type	Correlation Reference
Heat Transfer Correlations	
Air Side HTC	Wang-Tsai-Lu Wavy Smooth Louvered Fin
Refrigerant Liquid Phase HTC	Dittus Boelter
Refrigerant Two-phase HTC	Jung-Radermacher
Refrigerant Vapor Phase HTC	Dittus Boelter
Pressure Drop Correlations	
Air Side Pressure Drop	Wang-Tsai-Lu Wavy Smooth Louvered Fin
Refrigerant Liquid Phase	Blasius
Refrigerant Two-phase	Friedel
Refrigerant Vapor Phase	Blasius

Table 13: Input values for the evaporator model

Variable	Unit	Value
Air side		
Air Flow Rate	m^3/s	0.0393
Air Pressure	kPa	101.325
Air Temp.	°C	26.3
Air RH	%	50
Refrigerant side		
Evap. Saturation Temp.	°C	14.5
Evap. Inlet Quality	-	0.15
Mass Flow Rate	g/s	1.00

Table 13 shows the input values acquired from the test results except for the air side RH, which was assumed to be 50%. Table 14 is a summary of the comparison results.

Table 14 Comparison of the CoilDesigner and test results for the evaporator

Variables	Test Value	Modeling Value	Difference (%)
Air side			
Inlet Temp. (°C)	26.3	26.3	0
Outlet Temp. (°C)	22.7	22.9	0.9
Refrigerant side			
Outlet Temp. (°C)	22.5	24.6	9.3
Outlet Pressure (kPa)	481.3	480.4	-0.2
System			
Refrigerant Side Capacity (W)	165.6	168.6	1.8
Air Side Capacity (W)	172.8	168.6	-2.4

The modeling results were compared with the test data for both refrigerant side and air side. The results matched quite well, which validates the model in CoilDesigner. The model showed that among the 168.6 W total evaporator capacity, 159.0 W came from two-phase region heat transfer and 9.5 W was from the vapor region heat transfer. However, considering the total length of the evaporator, 40.8% of which was for two-phase region and the rest 59.2% was for vapor. This indicated that the evaporator used in the system was actually oversized. Small-size heat exchanger should be considered for next generation design.

PCM side

Figure 32 shows thermocouple locations in the PCM container. The detailed description on how the thermocouples were installed in the PCM was provided in the section PCM Thermocouple.

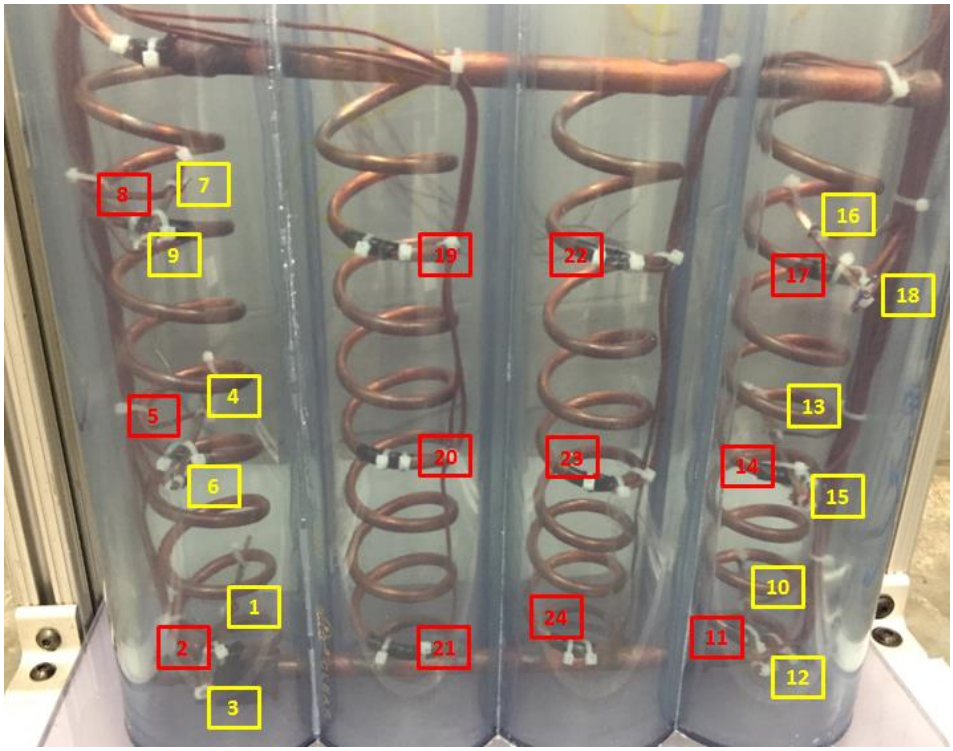

Figure 32: Thermocouple locations in the PCM container

Figure 33 shows the temperature measurement from the surface thermocouples attached to the copper tube (numbers shown in red in Figure 32) along the test period. Temperature started at 26°C, which was the room temperature. After about 30 minutes, temperature at different locations in the PCM reached a stable condition in the range of 43°C to 49°C. At about 90 minutes, temperatures continued to increase again.

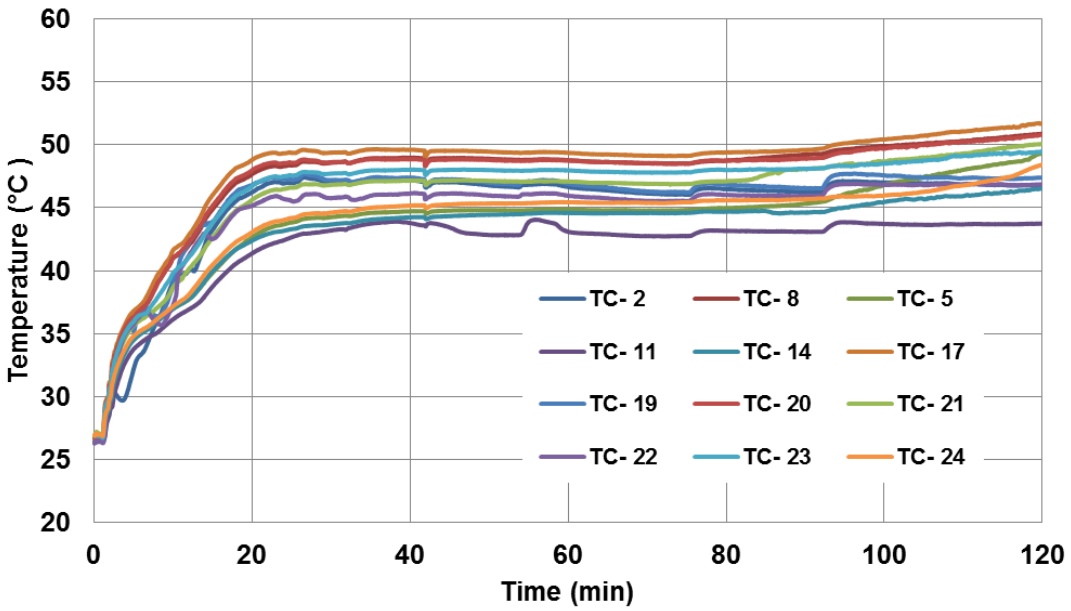

Figure 33: PCM temperatures at different locations

Figure 34 shows the temperature from four surface thermal couples at the upper level of the condenser. TC-8 and TC-17 were the ones attached to the left and right tubes and TC-19 and TC-20 were in the middle. An obvious gap was observed between these two groups. This was because the refrigerant was not distributed evenly into the four coils. The two coils on the side received more flow rate than the middle coils. In the future design of the PCM condenser, non-uniform flow distribution should be considered for the coils.

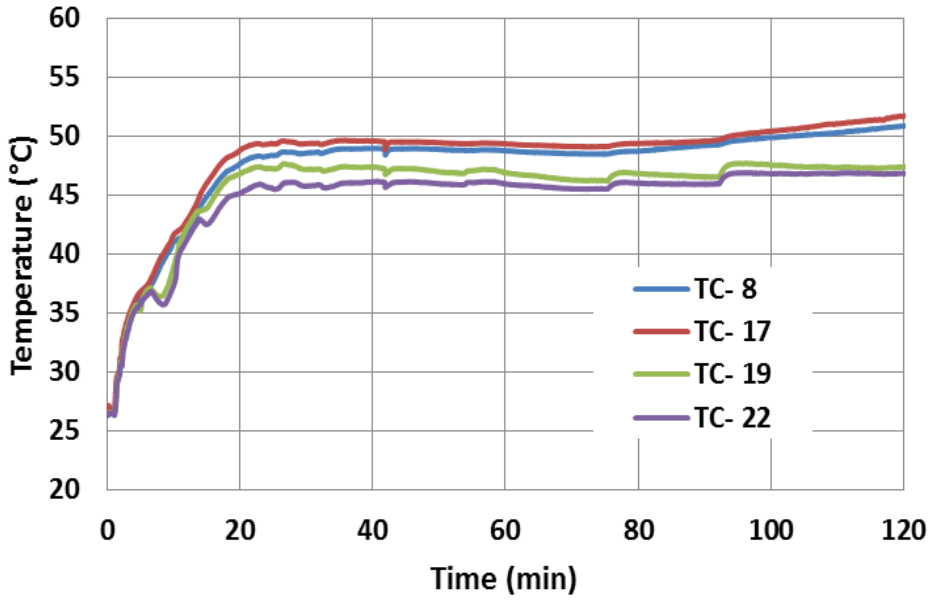

Figure 34: Copper tube surface temperatures at upper level

Figure 35 shows the temperature profiles of TC-7, TC-8 and TC-9. They were thermocouples on the upper level of the left coil. They were installed at the same height. TC-8 was on the copper tube surface. TC-7 was in the middle of the spiral tube and TC-9 was close to the container wall. Although TC-7 and TC-9 were symmetric to the copper tube, TC-9 temperature increased more slowly. The PCM container was insulated with foams, but there was still some heat loss from the container to the ambient air. This part of heat loss may be the reason that TC-9 temperature increase was not as much as TC-7 in the middle of the container.

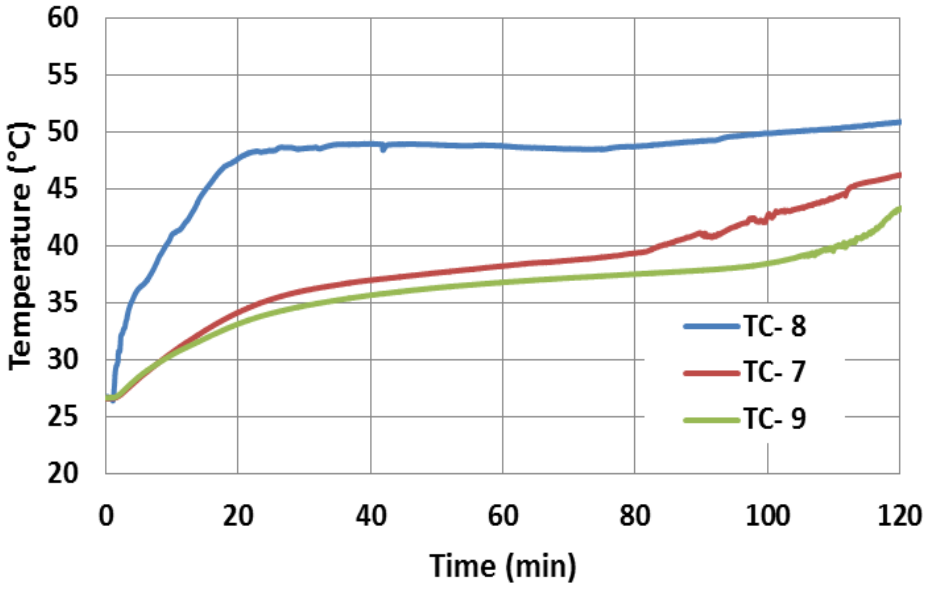

Figure 35: PCM temperatures at the same height (TC-8: copper tube surface; TC-7 inner center of spiral tube; TC-9: close-to-wall)

4.1.3 Energy Balance

In the refrigerant side of the vapor compression cycle, there were two major heat loss sections, as shown in

Figure 36. One was from the compressor discharge to condenser inlet, where the refrigerant was at the higher temperature in the cycle. The other section was from the condenser outlet to expansion valve inlet. Receiver and mass flow meter were installed in this liquid line, which were heat loss sources due to their bulky volume and large surface area.

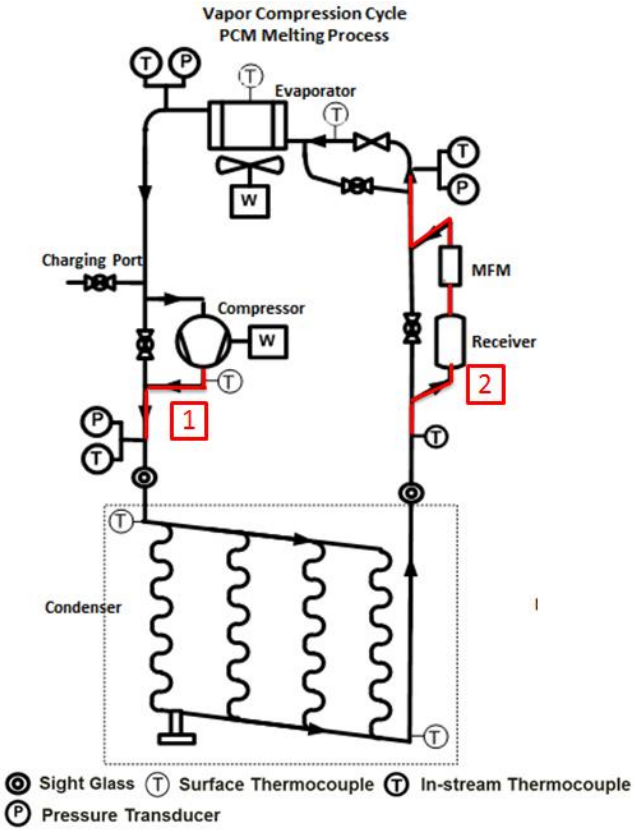

Figure 36: Heat loss sections in vapor compression cycle

The energy balance of the system was summarized in Table 15. In the refrigerant side, the compressor power and evaporator capacity were considered as heat input to the system. Heat output from the system included the condenser capacity and heat losses from the two sections mentioned above. From the calculation, the total heat input was 220.2 W and the total heat output was 191.7 W. The difference was 13%. In this energy balance calculation, the heat loss from the compressor surface directly to the ambient was not considered.

The evaporator capacity was calculated from both the refrigerant side and air side, and the difference was -4.4%. The energy balance for the vapor compression cycle was in an acceptable range.

Table 15: Energy balance summary of vapor compression cycle

Parameters	Unit	Value
Refrigerant Side		
Comp. Power	W	54.7
Evap. Capacity	W	165.5
Cond. Capacity	W	178.7
Heat Loss 1	W	9.4
Heat Loss 2	W	3.6
Heat Input	W	220.2
Heat Output	W	191.7
Difference	%	13.0
Air Side		
Evap. In Temp.	°C	26.3
Evap. Out Temp.	°C	22.7
Air Flow Rate	m^3/s	0.0393
Evap. Air Side Capacity	W	172.8
Energy Balance	%	-4.4

4.2 Baseline Thermosiphon Loop

After the two hours vapor compression cycle operation, the compressor was turned off while the fan was still on all the time during thermosiphon cycle. The three ball valves in the system were open. The liquid phase refrigerant stored in the receiver first flowed down into the evaporator (condenser in vapor compression cycle). After about 15 seconds, bubbles were observed in the sight glass from the riser and down flowing refrigerant appeared in the sight glass from the downcomer, which indicated the thermosiphon loop was working properly. The system was operated for about 750 minutes. At around 500 minutes, few bubbles were observed in the riser. This was

because the temperature difference between the evaporator and condenser decreased, so that the refrigerant circulation was slowed down. In this stage, natural convection was the major mechanism for the PCM to cool down.

4.2.1 Temperature Profile

Figure 37 shows the temperature profiles of the thermocouples attached to the surface of the copper tubes. At the beginning of the thermosiphon loop, the temperature difference between the evaporator and condenser was about 20°C. The heat transfer was very effective at this stage and the temperature was decreased to 37°C, which was the melting temperature of the PCM, in less than 5 minutes. After that, the temperature decreased gradually to around 29°C in 400 minutes. Then, the temperature drop slowed down and natural convection dominated the heat transfer from the PCM to the ambient.

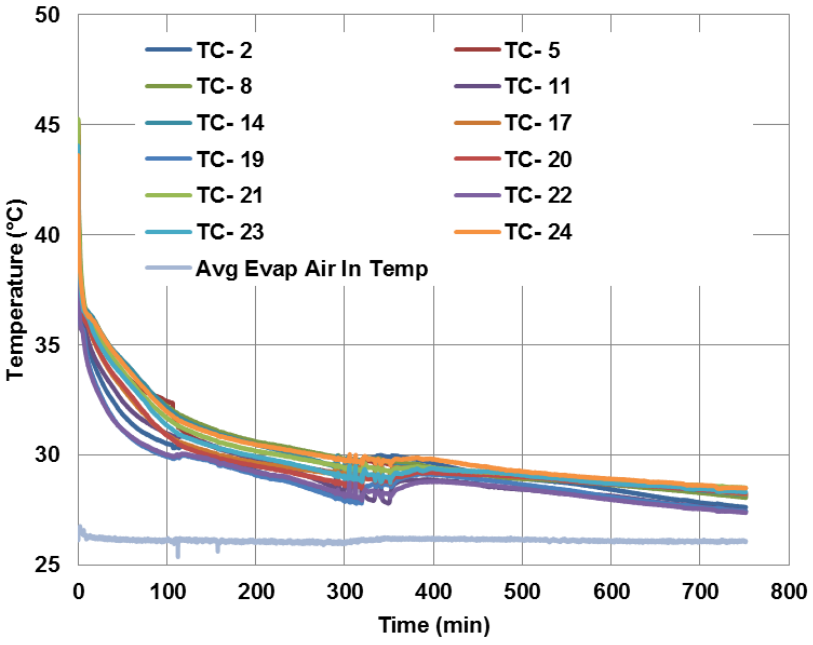

Figure 37: Copper tube surface temperature during the PCM solidification process

Figure 38 shows the temperature from left coil of the evaporator at upper level (TC-8 on the surface of the copper tube, TC-9 in the middle of the spiral tube, TC-7 close to the wall). Center of the spiral tube was the location being cooled last. It can be also observed that at around 500 minutes, the temperatures at these locations were the same, which meant thermosiphon no longer worked and the rest of the sensible heat of the PCM was released to the ambient through natural convection.

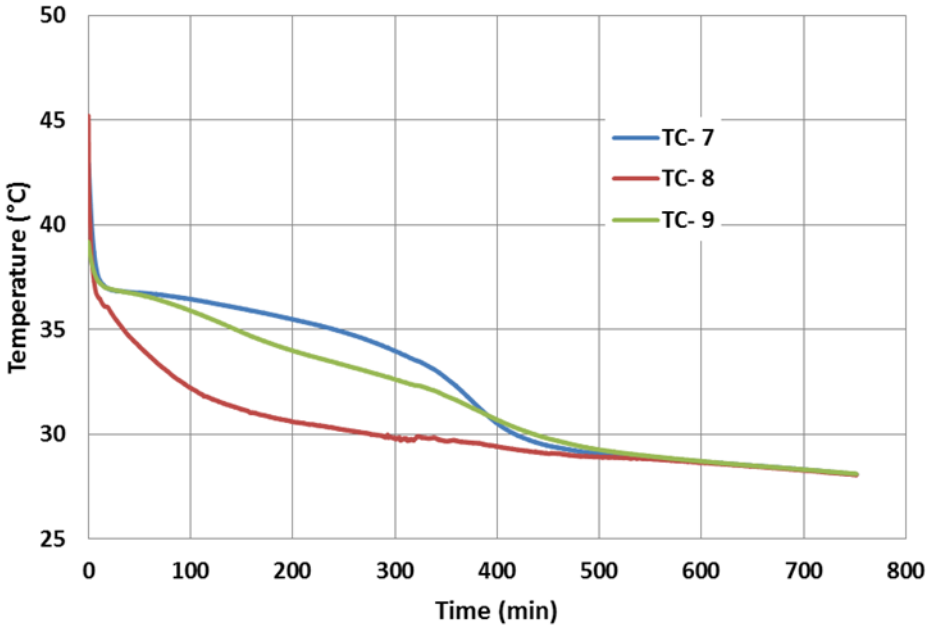

Figure 38: Temperature at the upper level of the left coil during PCM solidification process

4.2.2 Energy Balance

Thermocouples were installed in the evaporator inlet and outlet from the air side to measure the air temperature change. From the temperature difference of the air, condenser air side capacity was calculated.

Figure 39 shows the condenser air side temperature and the condenser capacity. The air inlet temperature was around 26°C, which was the setting temperature for the chamber. The condenser capacity decreased very fast in the first 500 minutes from

around 160 W to 13 W. After 500 minutes, the capacity was constant at around 13 W. At this stage, the temperature difference was less than 0.5°C, which was even in the range of the temperature measurement uncertainty. The other reason that may cause the evaporator outlet air temperature a little bit higher than that at the inlet, may be the heat generated from the fan motor. Based on this reason, it was concluded that after 500 minutes, the thermosiphon cycle did not work. Based on this, the condenser capacity at 500 minutes was assumed to be 0 W. And the 13 W condenser capacity was deducted from the all previous recorded data to disregard the part of heat generated by the fan.

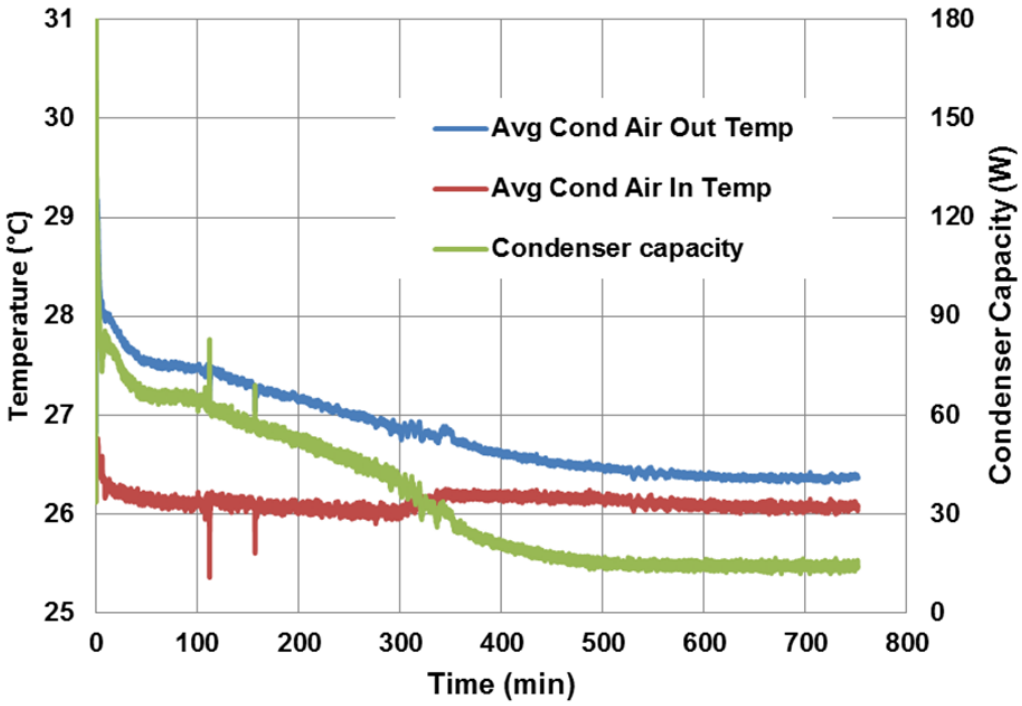

Figure 39: Condenser air side temperature and condenser capacity during PCM solidification process

Under this assumption, a plot of energy balance between vapor compression cycle and thermosiphon loop was shown in Figure 40. The blue line indicated the total

energy that was discharged from the condenser (evaporator in the thermosiphon loop). This was calculated by integrating the condenser capacity from the refrigerant side with time. Then the condenser capacity (evaporator in the vapor compression cycle), shown in red line in the figure, was also integrated with around 750 minutes of running time. The accumulated removed energy from the thermosiphon system was shown in the green line. At the end of 750 minutes, the total heat removed from the thermosiphon system from the condenser air side capacity calculation was 0.91 MJ. The difference between the total heat stored in the PCM in the vapor compression cycle was 18.3%. This energy balance result could be due to the heat loss from the system to the ambient during the 750 minutes running time.

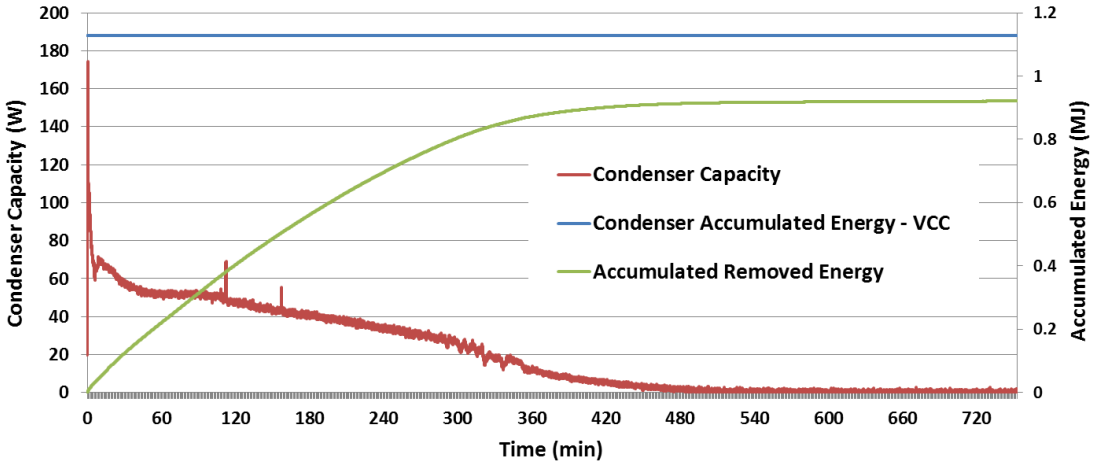

Figure 40: Energy balance between vapor compression cycle the thermosiphon loop

The overall system COP was evaluated for both the vapor compression cycle and thermosiphon loop. The operation time for the thermosiphon was 500 minutes. After that, air-side condenser capacity didn't change. The evaporator capacity, compressor and fan powers were integrated with time during the vapor compression cycle operation. Total energy consumption of the fan during the thermosiphon loop was also considered for the system overall COP. The results are summarized in Table 16.

Table 16: Overall system COP during vapor compression cycle and thermosiphon loop for baseline test facility

System Mode	Operation Time [min]	Component	Energy Consumption [MJ]
Vapor Compression Cycle	**120**	**Evaporator**	**1.044**
		Compressor	**0.380**
		Fan	**0.024**
Thermosiphon	**500**	**Fan**	**0.103**
Overall System COP: 2.06			

4.3 System Test with Battery Pack

System was also tested with battery pack with the same refrigerant charge. The test data with a battery pack was averaged for the same time period and compared with the 24V DC power supply case in Table 17.

Table 17: Comparison of tests with two power sources

Properties	24V Power Supply	Battery Pack	Absolute Uncertainty
Suction Pressure [kPa]	481.3	481.4	1.7
Discharge Pressure [kPa]	1336.8	1319.9	8.6
Evaporating Temp. [°C]	15.2	15.2	0.5
Condensing Temp. [°C]	50.5	50.0	0.5
Mass Flow Rate [g/s]	1.00	1.00	0.001
Superheat [K]	8.0	7.2	0.5
Subcool [K]	7.4	6.3	0.5
Compressor Power [W]	54.7	54.2	0.8
Evaporator Capacity [W]	165.6	164.1	0.9
System COP [-]	2.85	2.85	0.04

The system with battery pack had similar performance as one with 24 V power supply. The test was conducted for two hours and the voltage of the battery pack was recorded, as shown in Figure 41. During the two hours running time, the voltage was decreased from 28.7 V to 25.8 V. The battery pack had enough energy to power the system for two hours.

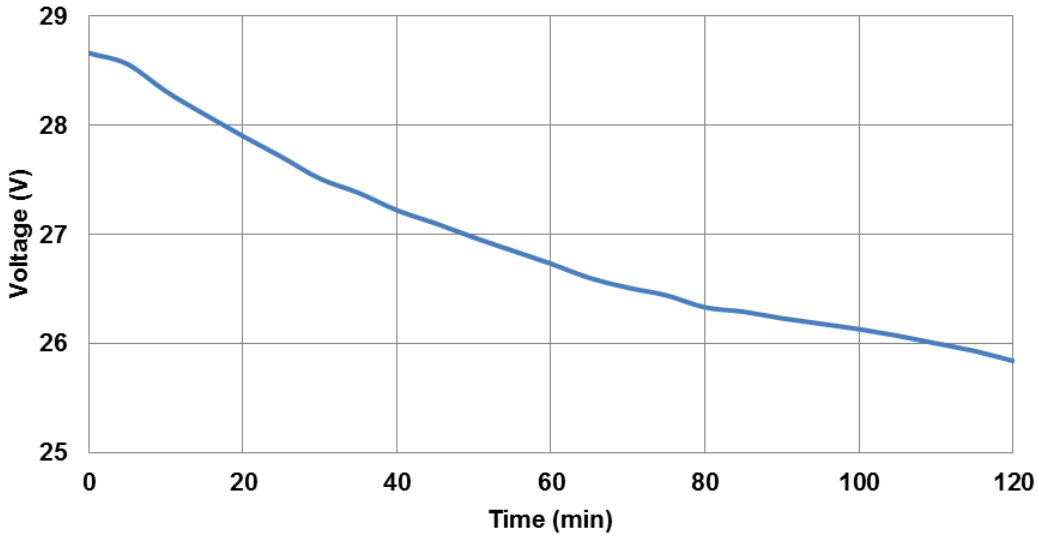

Figure 41: Battery pack voltage during vapor compression cycle

4.4 Prototype Performance

4.4.1 System Description

Based on the baseline test results, a prototype was designed, built and tested.

The main system components like compressor, evaporator, condenser, expansion valve, PCM and PCM container remained the same as in the baseline.

Receiver was re-designed, as shown in Figure 42, to fit in the limited space in the prototype. It was made of five straight copper tubes with 6.4 mm O.D. tubes

connected. The height of each tube was 12 cm. It was able to store 200 g refrigerant inside.

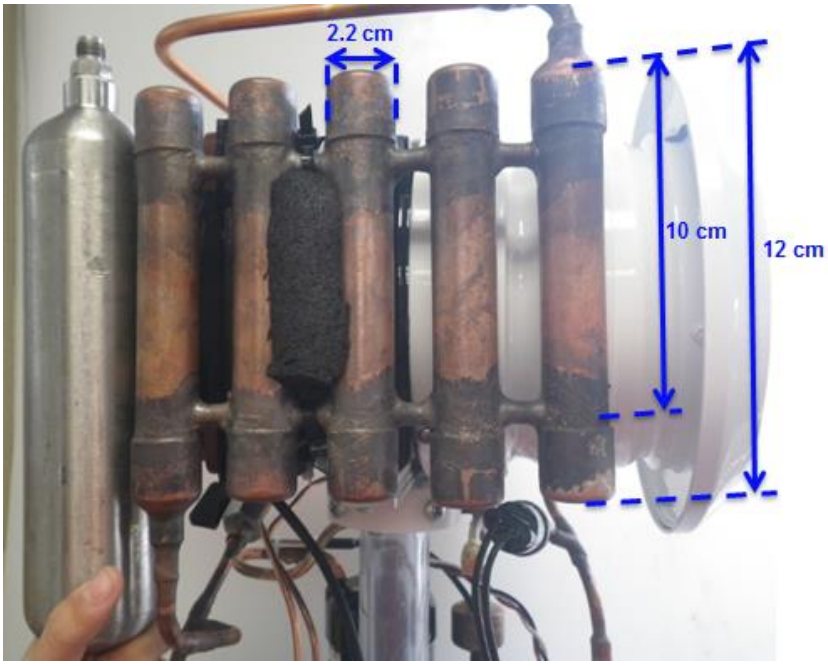

Figure 42: Receiver in the prototype

A PCM container with the same inner dimension was 3D printed to fit on the 35.6 cm bottom plate, as shown in Figure 43. Condenser was twisted in spiral shape to fit into the PCM container, as shown in

Figure 44. The positions where PCM last melted and solidified were determined from the baseline test. Therefore, temperature sensors were installed as indicators to show PCM was fully melted or fully solidified.

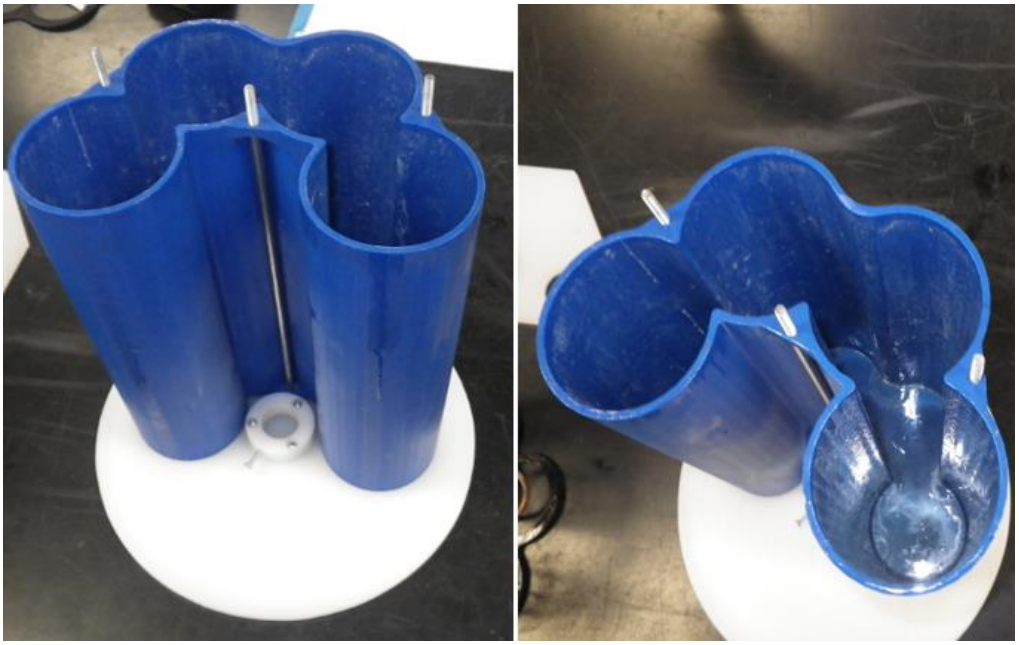

Figure 43: 3D printed PCM container

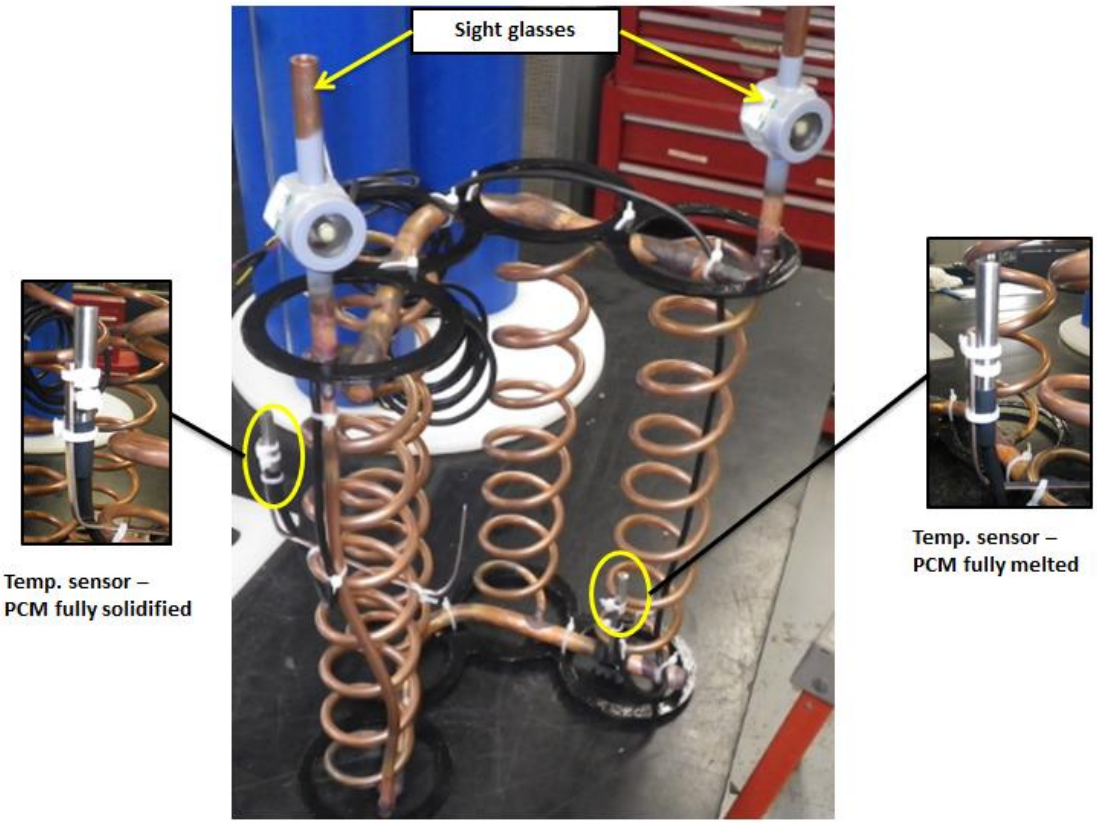

Figure 44: Condenser in the prototype

A nozzle with 8 cm outlet dimension was assembled with evaporator and fan in the prototype, as shown in

Figure 45. The final assembly of the prototype was shown in

Figure 46.

Figure 45: Nozzle-evaporator-fan assembly in the prototype

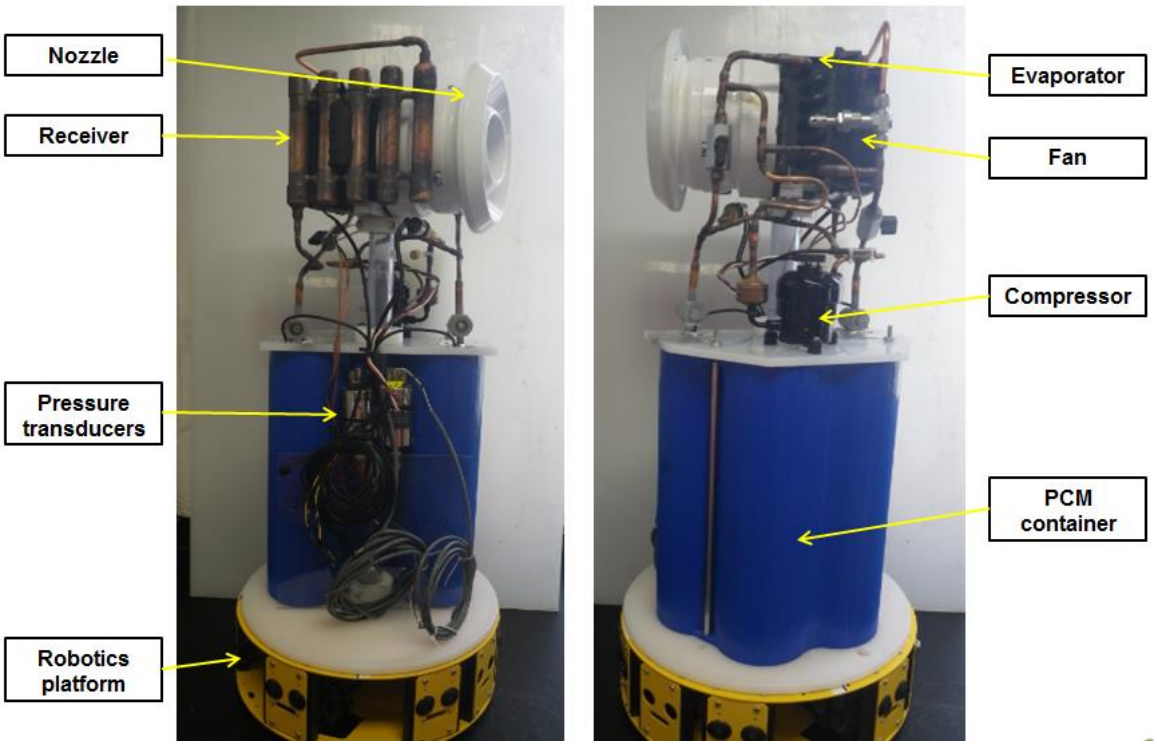

Figure 46: Prototype assembly

The prototype was also equipped with some safety features, as shown in Figure 47. A surface thermocouples were attached at the compressor discharge. When the measured temperature exceeds 80°C, the compressor is turned off automatically. The pressure switch was also installed to shut down the system when the discharge pressure exceeded 1,700 kPa.

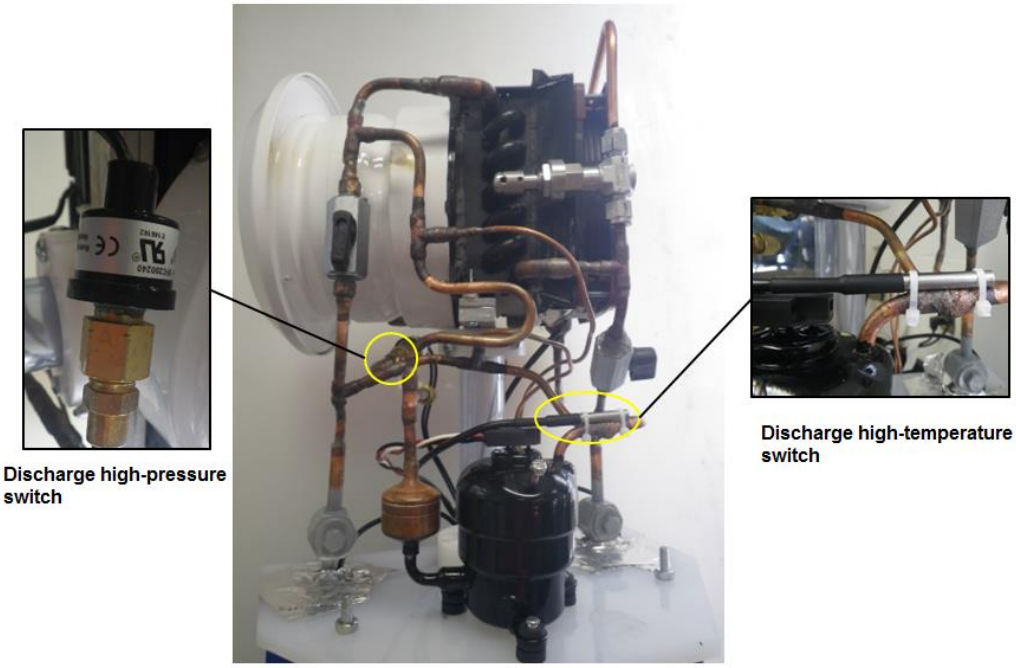

Figure 47: High temperature and pressure safety switches in prototype

4.4.2 Vapor Compression Cycle

In addition to the two pressure transducers installed in the compressor suction line and discharge, six surface thermocouples were attached to the surface of the copper tube to measure the refrigerant temperature, as shown in Figure 48. The same battery pack was used as power supply for the prototype as in the baseline test. The voltage of the battery pack was measured and recorded. The current went through the

compressor control board and battery pack was also measured to calculate the power consumption of the compressor and whole system.

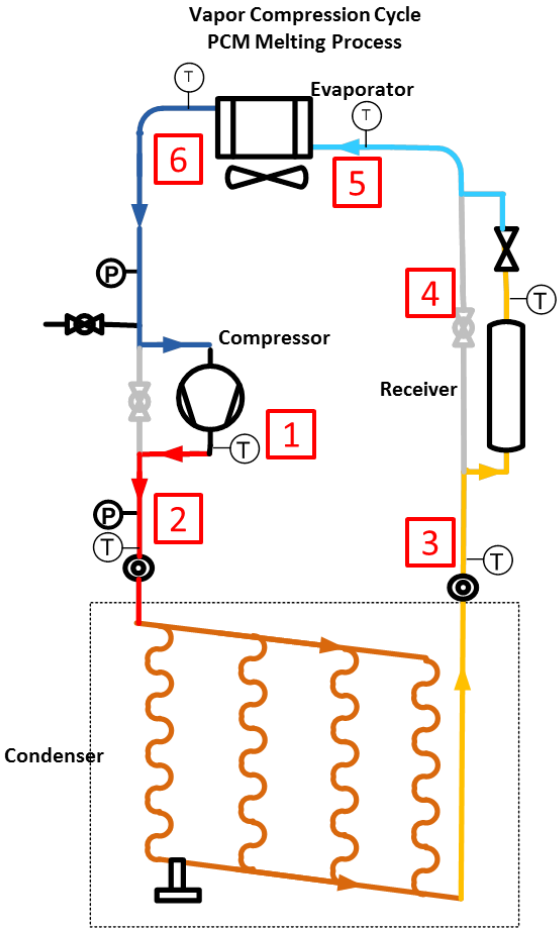

Figure 48: Prototype schematic

The total refrigerant charge of the prototype was 398 g and the system was running for two hours. For the prototype, the expansion valve was not manually regulated to maintain the superheat as done in the baseline test. It was at the same opening throughout the test. The suction and discharge pressures were shown in Figure 49. It had the same trends as in the baseline test. There was a 25 minutes start up process for the system. In the process, refrigerant gradually filled the receiver. After that, the system went into a stable process.

No mass flow meter was installed in the prototype, so the evaporator capacity was calculated only from the air side temperature difference and air flow rate. The air flow rate was measured to be 0.025 m^3/s. Based on that, the mass flow rate from the refrigerant side can be calculated. The evaporator air side temperature profile was shown in Figure 50. The room temperature was set 26°C. There were some fluctuation of the temperature in the air side but in general they were stable

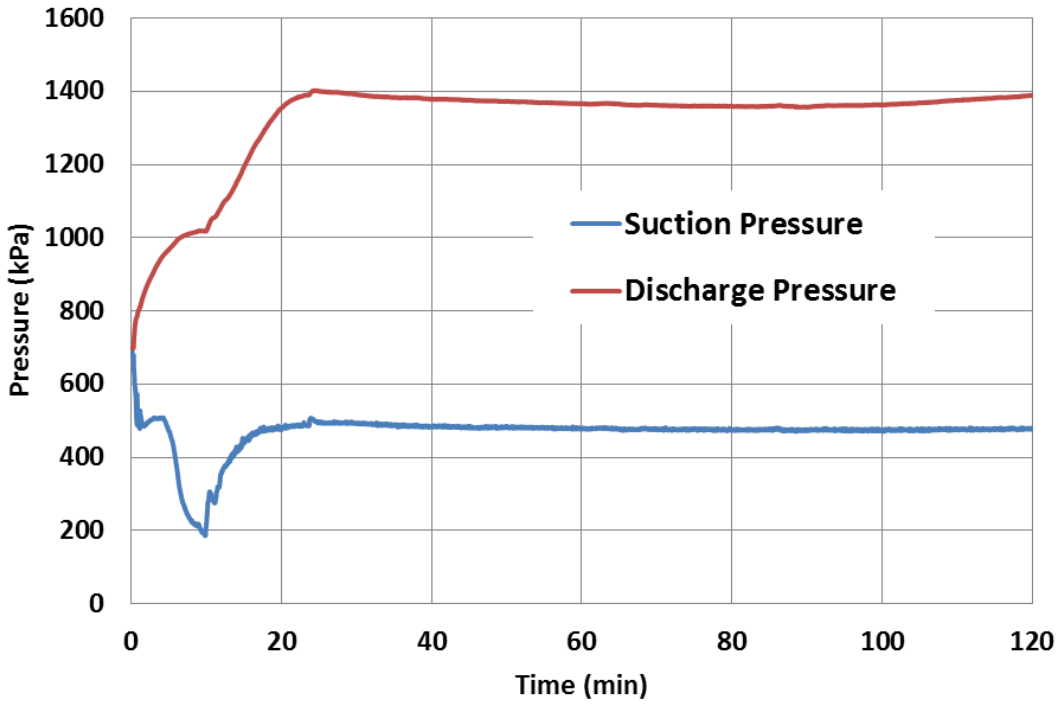

Figure 49: Refrigerant-side pressures during vapor compression cycle test for prototype

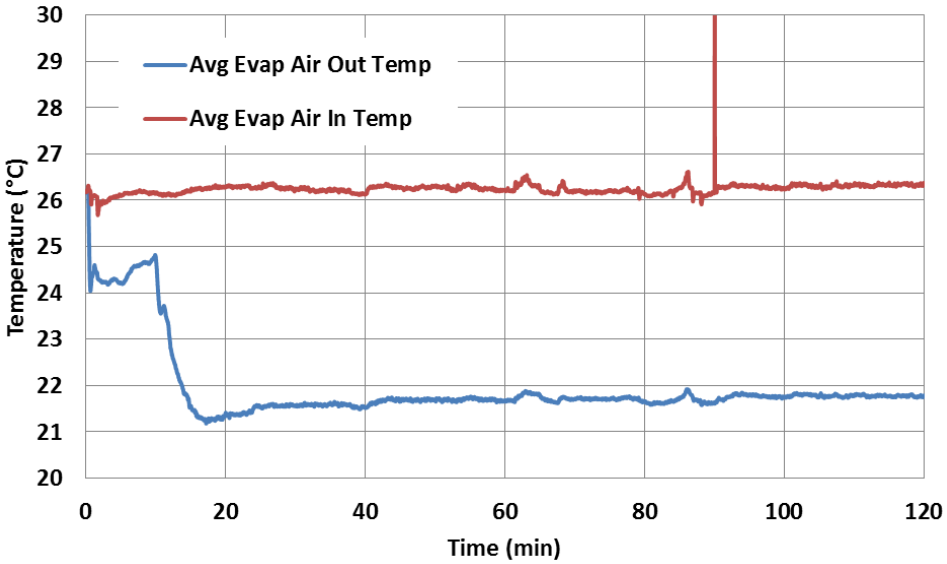

Figure 50: Evaporator airside inlet and outlet temperatures

The vapor compression cycle was powered by the battery pack and the voltage of the battery pack was recorded in Figure 51. The original voltage of the battery pack when fully charged was 29.7 V. After a two hours test, it still had the voltage value at 25.6 V, which indicated the energy of the batter pack was sufficient for the two hours test.

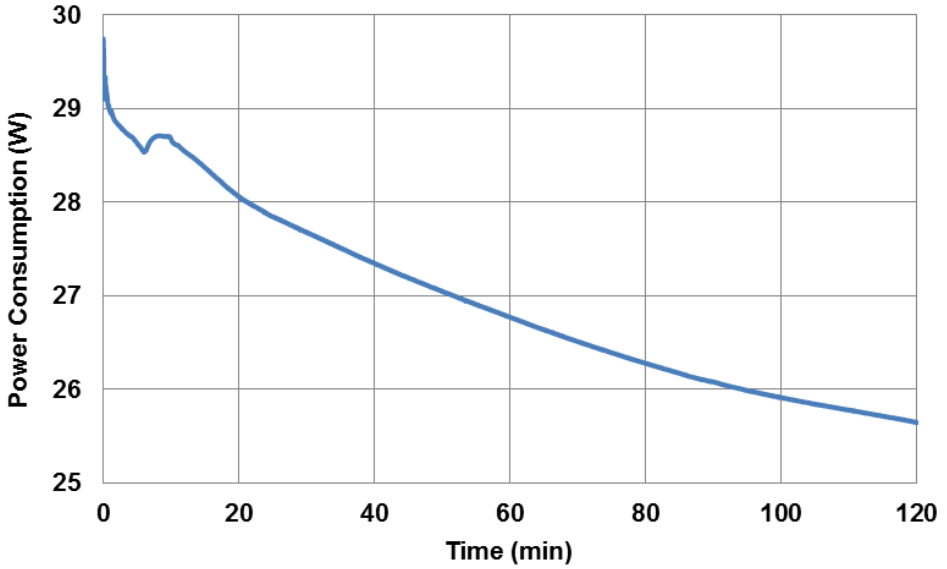

Figure 51: The voltage of the battery power during the prototype test

Test data from 50 minutes to 80 minutes during stabilization period was averaged, as shown in Table 18. The air side temperature difference was 4.5 K. The evaporator capacity was 136.2 W. Since the calculation was based on the air temperature difference, there was an uncertainty of 10.7 W. System COP was 2.2 for the prototype test.

Table 18: System performance of the prototype during the stabilization period

Variable	Unit	Prototype	Absolute Uncertainty
Suction Pressure	kPa	478.5	1.7
Discharge Pressure	kPa	1,365.0	8.6
Air Inlet Temp.	°C	26.2	0.25
Air Outlet Temp.	°C	21.7	0.25
Mass Flow Rate	g/s	0.78	0.06
Superheat	K	9.5	0.5
Subcool	K	12.2	0.5
Comp. Power	W	54.0	0.8
Evap. Capacity	W	136.2	10.7
System COP	-	2.2	0.17

Considering the refrigerant side energy balance, there were two major heat loss sections. One was from the compressor discharge to the condenser inlet, where the refrigerant was with highest temperature in the cycle (refer as heat loss 1). The other section was from the condenser out let to the expansion valve inlet because of the large surface area of the receiver (refer as heat loss 2). A summary of the energy balance is shown in Table 19. The heat input to the system was the sum of compressor power and evaporator capacity while the condenser capacity and heat

losses counted for the heat output from the vapor compression cycle. The difference was 18%. There was portion of the heat loss from the hot compressor surface directly to the ambient air. Other heat loss through the suction line from the evaporator outlet to the compressor suction was not considered here. Besides, the refrigerant side temperature measurement was based on surface thermocouples, which has a higher uncertainty than with the in-stream thermocouples. These were the factors which contributed to the energy unbalance from the refrigerant side.

Table 19: Summary of the energy balance from the refrigerant side

Parameters	Unit	Value
Comp. Power	W	54.0
Evap. Capacity	W	136.1
Cond. Capacity	W	139.4
Heat Loss 1	W	4.4
Heat Loss 2	W	11.2
Heat Input	W	190.1
Heat Output	W	155
Difference	%	18.5

4.4.3 Thermosiphon Loop

After two hours vapor compression cycle test, two ball valves were closed and the compressor was turned off. The fan was remained on during the thermosiphon loop. The air side temperature profile at the condenser inlet and outlet, and the capacity were shown in Figure 52. The condenser had a very high capacity at the beginning, due to the large temperature difference between the condenser and evaporator. Then it decreased from 150 W to around 13 W. According to the baseline test observation,

this indicated the end of thermosiphon and the rest sensible heat would be slowly removed by natural convection.

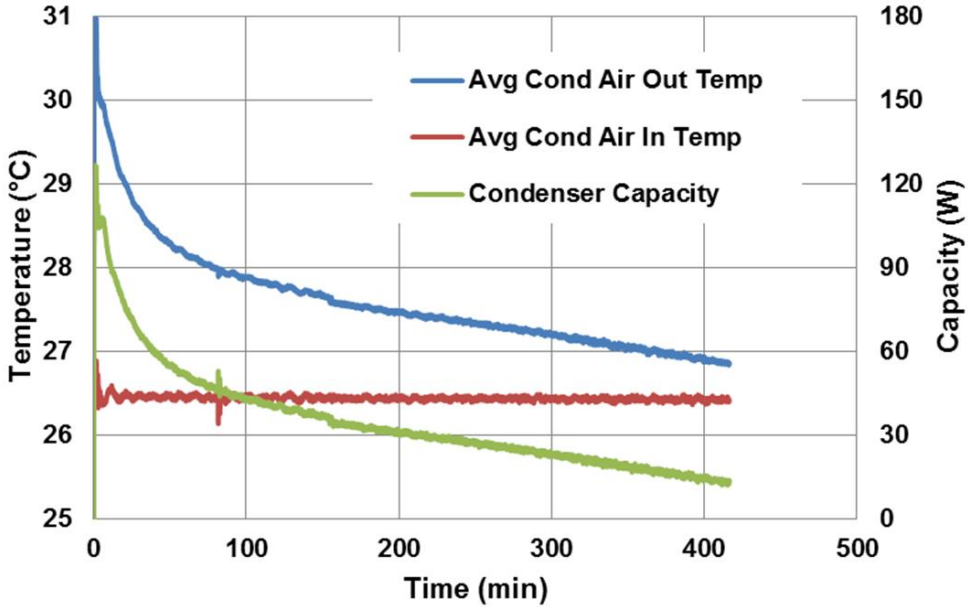

Figure 52: Condenser air-side temperature and condenser capacity during PCM solidification process of prototype

4.4.4 Comparison with Baseline Test

Compared with the baseline test, the prototype was built with the same main components: compressor, evaporator, condenser, expansion valve and fan. However, the fan in the prototype was integrated with evaporator and nozzle, which resulted in a larger air side pressure drop and a decreased air flow rate. A detailed comparison of the performances of the baseline test (with battery pack as power supply) and the prototype is shown in Table 20.

Table 20: System performance comparison from the baseline test and prototype

Properties	Baseline	Prototype
	Refrigerant Side	
Suction Pressure [kPa]	481.4	478.5
Discharge Pressure [kPa]	1,319.9	1,365.0
Evaporating Temp. [°C]	15.2	14.4
Condensing Temp. [°C]	50.0	51.4
Mass Flow Rate [g/s]	1.00	0.78
Superheat [K]	7.2	9.5
Subcool [K]	6.3	12.2
Compressor Power [W]	54.2	54.0
Evaporator Capacity [W]	164.1	136.1
System COP [-]	2.85	2.2
	Air Side	
Air In Temp. [˚C]	26.3	26.2
Air Out Temp. [˚C]	22.7	21.7
Air Flow Rate [m^3/s]	0.039	0.025
	Battery	
Start Voltage [V]	29.1	29.7
End Voltage [V]	25.8	25.6

Chapter 5: Conclusions

With an increasing demands for saving energy in space cooling and improving thermal comfort, a battery powered portable vapor compression cycle air conditioning device was designed, developed and tested. R-134a was used as working fluid in the system. The designed cooling time was two hours for the system. It was operated in two modes: one was cooling mode, the other was recharging mode. For the cooling, the system worked as a vapor compression cycle. The condenser of the system was submerged in the PCM so that the heat from the condenser could be stored the PCM as latent heat. For the recharging mode, the compressor was turned off and the fan was kept operated while the compressor and expansion valve in the vapor compression cycle were bypassed so that the system worked as a closed loop two-phase thermosiphon loop. The heat from the PCM was removed and released to the air by the thermosiphon and PCM solidified in this process.

A baseline test facility was set up to evaluate the system performance. Instruments were installed into the facility to measure the thermodynamic properties of the system. The baseline vapor compression cycle was operated for two hours under 26°C ambient setting temperature. The averaged system cooling capacity was 165.6 W during stabilization period with a COP of 2.85. The expansion valve was manually regulated to maintain the superheat between 5 and 8 K during the test period. The evaporator outlet air temperature was 22.7°C, with a 3.6°C temperature drop from the measured inlet air temperature. The energy balance between the evaporator air side and refrigerant side capacities was checked and the difference was 4.4%, which showed an acceptable energy balance for the vapor compression cycle. A 7s3p battery

pack was used as the power supply during the test and the voltage output after the vapor compression cycle operation was 25.8 V, which indicated sufficient energy supply for the battery pack used.

The recharging thermosiphon mode of the baseline was conducted after the vapor compression cycle. Bubbles were observed in the sight glass in the riser and down flowing refrigerant appeared in the sight glass in the downcomer. The condenser (working as an evaporator in the vapor compression cycle mode) capacity dropped very fast in the first 500 minutes from around 160 W to 13 W when the temperature difference between the evaporator and condenser was less than 0.5°C. After that, the convection mode dominated the heat transfer process to remove the sensible heat from the PCM. The energy balance between the vapor compression cycle and thermosiphon loop was also investigated. The condenser capacity measured in the vapor compression cycle was integrated with time to calculate the total heat stored in the PCM, which was 1.12 MJ in the test. In the thermosiphon loop, the calculated total heat removed from the PCM was 0.91 MJ based on the air side temperature difference. The difference between the energy stored and discharged in the PCM was 18.3%. Considering the 750 minutes running time and the possible heat loss from the system to ambient, the energy balance was in a reasonable range.

After the baseline test, a prototype was designed, built and tested. It included the same main components as in the baseline test. However, the evaporator and fan were integrated with a nozzle, which resulted in more air side pressure drop and less evaporator capacity. The measured air side averaged evaporator capacity was 136.3 W with system COP of 2.2. The air side temperature difference was 4.5°C.

Thermosiphon mode worked for the prototype as well and it took about 420 minutes to bring down the air side temperature difference at the evaporator within 0.5°C. The same battery pack served as the power supply for the prototype and the voltage after the vapor compression cycle operation was 25.6 V.

The system performance of the vapor compression cycle system with PCM condenser operated in thermosiphon loop during the charging mode was experimentally investigated in this thesis. The results indicated the potential of applying the prototype to personal cooling device indoors.

The main contributions of this thesis are summarized as below:

- Calculated and designed a heat exchanger that merged into PCM as the condenser for vapor compression cycle and evaporator for thermosiphon system
- Designed, fabricated and tested a novel battery powered portable vapor compression cycle personal cooling system with PCM condenser
- Designed and integrated the thermosiphon mode for the cooling system to efficiently remove the heat from PCM
- Built the first prototype for RoCo and validated the expected performance of it

Chapter 6: Future Work

For the current system design, due to the poor heat transfer from the condenser to the PCM, an oversized condenser was designed. This contributed to the charge unbalance between the vapor compression cycle and thermosiphon loop. A receiver was installed to solve the problem in current study. However, this resulted in longer startup time to reach to the stabilization condition and more charge is demanded for the system. For the future work, there are two possible approaches to address these issues. One is to enhance the heat transfer between the condenser to the PCM such as replacing the current copper tube with tube-and-fin heat exchanger or microchannel heat exchanger. The other approach is to improve the PCM conductivity. One effective way to do so is to integrate the graphite grid into the current PCM. The optimizing the PCM condenser design is the next step to improve the system performance.

During the operation for the baseline test, the expansion valve was be manually regulated to maintain the proper superheat for the system. For future design, more advanced expansion devices such as thermostatic expansion valve or electronic expansion valve can be used for superheat control.

Air flow rate from the evaporator side was not accurately measured in current baseline test facility and prototype. In the baseline test facility, the air flow rate was calculated from the fan power consumption. For the prototype, the air velocity was measured by digital anemometer in different locations at a grid matrix. The air velocity profile was integrated with the corresponding area to get the air flow rate. In the future test, an air duct with electric heater is recommended. By measuring the duct

inlet and outlet temperature difference and the electric heater power consumption, the air flow rate from the evaporator side can be determined more accurately.

The achieving a target cooling performance of the system was focused in this study. In order to provide thermal comforts around the year, the heating mode of the device should be developed as well.

Bibliography

[1] "Annual Energy Outlook," U.S. Energy Information Administration, 2015.

[2] "California Energy Commission," [Online]. Available: http://www.consumerenergycenter.org/tips/summer.html. [Accessed 3 3 2016].

[3] J. Berko, D. D. Ingram, S. Saha and P. D. Jennifer, "Deaths Attributed to Heat, Cold, and Other Weather Events in the United States, 2006–2010," National Center for Health Statictics, 2014.

[4] Y. M. Motahareh and S. Mohammad , "Personal cooling garments: a review," *Journal of The Textile Institute,* vol. 105, no. 12, pp. 1231-1250, 2014.

[5] "COOL ON THE GO," [Online]. Available: http://www.coolonthego.com/. [Accessed 3 3 2016].

[6] T. M. McLellan, "The efficacy of an air-cooling vest to reduce thermal strain for Light Armour Vehicle personnel," Defence R&D Canada, 2007.

[7] M. F. Mohammed, M. K. Amar, A. K. R. Siddique and A.-H. Said, "A review on phase change energy storage: materials and applications," *Energy Conversion and Management,* vol. 45, no. 9-10, pp. 1597-1615, 2004.

[8] J. R. House, H. C. Lunt, R. Taylor, G. Milligan, J. A. Lyons and C. M. House, "The impact of a phase-change cooling vest on heat strain and the effect of different cooling pack melting temperatures," *European Journal of Applied Physiology,* vol. 113, no. 5, pp. 1223-1231, 2013.

[9] Kalev Kuklane, Karin Lundgren, Chuansi Gao and Jakob Löndahl, "Ebola:

Improving the Design of Protective Clothing for Emergency Workers Allows Them to Better Cope with Heat Stress and Help to Contain the Epidemic," *The Annals of Accupational Hygiene,* vol. 59, no. 2, pp. 258-261, 2015.

[10] E. Y, S. Y and B. S., "Comparison between different auxiliary cooling devices in a severe hot/dry climate," *Ergonomics,* vol. 29, no. 1, p. 41, 1986.

[11] "C2 climate control," 2007. [Online]. Available: http://www.hermanmiller.com/hm/content/product_showroom/shared_assets/files/bro_thebecollection_c2.pdf. [Accessed 3 3 2016].

[12] T. C. Ernsta and S. Garimella, "Demonstration of a wearable cooling system for elevated ambient temperature duty personnel," *Applied Thermal Engineering,* vol. 60, no. 1-2, pp. 316-324, 2013.

[13] A. F. Regin, S. Solanki and J. Saini, "Heat transfer characteristics of thermal energy storage system using PCM capsules: A review," *Renewable and Sustainable Energy Reviews,* vol. 12, no. 9, pp. 2438-2458, 2008.

[14] S. E. Kalnæsa and B. P. Jelle, "Phase change materials and products for building applications: A state-of-the-art review and future research opportunities," *Energy and Buildings,* vol. 94, pp. 150-176, 2015.

[15] PCM Energy P. Ltd, [Online]. Available: http://pcmenergy.com/products.htm. [Accessed 3 3 2016].

[16] M. Medranoa, M. Yilmazb, M. Nogués a, I. Martorella, J. Rocaa and L. F. Cabeza, "Experimental evaluation of commercial heat exchangers for use as PCM thermal storage systems," *Applied Energy,* vol. 86, no. 10, pp. 2047-2055,

2009.

[17] A. Trp, "An experimental and numerical investigation of heat transfer during technical grade paraffin melting and solidification in a shell-and-tube latent thermal energy storage unit," *Solar Energy,* vol. 79, no. 6, pp. 648-660, 2005.

[18] A. Erek, Z. Illken and M. A. Acar, "Experimental and numerical investigation of thermal energystorage with a finned tube," *INTERNATIONAL JOURNAL OF ENERGY RESEARCH,* vol. 29, pp. 283-301, 2005.

[19] M. Rahimia, A. Ranjbara, D. Ganjia, K. Sedighia, M. Hosseinib and R. Bahrampoury, "Analysis of geometrical and operational parameters of PCM in a fin and tube heat exchanger," *International Communications in Heat and Mass Transfer,* vol. 53, pp. 109-115, 2014.

[20] X. Zhang, S. Yu, M. Yu and Y. Lin, "Experimental research on condensing heat recovery using phase change material," *Applied Thermal Engineering,* vol. 31, no. 17-18, pp. 3736-3740, 2011.

[21] Y. Dobriansky, "Concepts of self-acting circulation loops for downward heat transfer (reverse thermosiphons)," *Energy Conversion and Management,* vol. 52, no. 1, pp. 414-425, 2011.

[22] A. Franco and S. Filippeschi, "Closed Loop Two-Phase Thermosyphon of Small Dimensions: a Review of the Experimental Results," *Microgravity Science and Technology,* vol. 24, no. 3, pp. 165-179, 2011.

[23] H. Abou-Ziyana, A. Helalia, M. Fatouha and M. El-Nasr, "Performance of stationary and vibrated thermosyphon working with water and R134a," *Applied*

Thermal Engineering, vol. 21, no. 8, pp. 813-830, 2001.

[24] K. Ong and M. Haider-E-Alahib, "Performance of a R-134a-filled thermosyphon," *Applied Thermal Engineering,* vol. 23, no. 18, pp. 2373-2381, 2003.

[25] R. Khodabandeh and R. Furberg, "Instability, heat transfer and flow regime in a two-phase flow thermosyphon loop at different diameter evaporator channel," *Applied Thermal Engineering,* vol. 30, no. 10, pp. 1107-1114, 2010.

[26] C. Ong and J. Thome, "Macro-to-microchannel transition in two-phase flow: Part 1 – Two-phase flow patterns and film thickness measurements," *Experimental Thermal and Fluid Science,* vol. 35, no. 1, pp. 37-47, 2011.

[27] P. Zhang, B. Wang, W. Shi and X. Li, "Experimental investigation on two-phase thermosyphon loop with partially liquid-filled downcomer," *Applied Energy,* vol. 160, pp. 10-17, 2015.

[28] V. Gnielinski, "New equations for heat and mass transfer in turbulent pipe and channel flow," *International Chemical Engineering,* vol. 16, pp. 359-368, 1976.

[29] P. R. H. BLASIUS, "Das Aehnlichkeitsgesetz bei Reibungsvorgangen in Flüssigkeiten," *Forschungsheft ,* vol. 131, pp. 1-41, 1913.

[30] M. M. Shah, "An Improved and Extended General Correlation for Heat Transfer During Condensation in Plain Tubes," *HVAC&R RESEARCH,* vol. 15, no. 5, pp. 889-913, 2009.

[31] J. R. Thome, "Chatper 17 Void Fractions in Two-Phase Flows," in *Engineering Data Book III,* Lausanne, Swiss Federal Institute of Technology Lausanne,

2010, pp. 17-4.

[32] Y. Cengel, "Chapter 8: Internal Forced Convection," in *Heat Transfer: A Practical Approach*, McGraw-Hill, 2003, pp. 419-452.

[33] G. K. Filonenko, "Hydraulic resistance in pipes," *Teploenergetika,* vol. 1, pp. 40-44, 1954.

[34] D. K. Edwards, V. E. Denny and A. F. Mills, Transfer Processes: An Introduction to Diffusion, Convection and Radiation, McGraw-Hill , 1979.

[35] Y. Jina, Q. Wan and Y. Dingb, "PCMs Heat Transfer Performance Enhancement with Expanded Graphite and its Thermal Stability," *Procedia Engineering,* vol. 102, pp. 1877-1884, 2015.

[36] A. Sathe, E. Groll and S. Garimella, "Experimental Evaluation of a Miniature Rotary Compressor for Application in Electronics Cooling," in *International Compressor Engineering Conference*, 2008.

[37] "A sophisticated tool for design and optimization of air-cooled heat exchangers," Center for Environmental Energy Engineering, University of Maryland, [Online]. Available: http://www.ceee.umd.edu/consortia/isoc/coil-designer. [Accessed 3 3 2016].